Journal of Manufacturing Processes 131 (2024) 93–110

Contents lists available at ScienceDirect

Journal of Manufacturing Processes

journal homepage: www.elsevier.com/locate/manpro

Electrical conductivity field analysis: A prognostic instrument for real time monitoring of friction stir welding process

Mattia Mazzeschi [a,*], Miguel Sanz [b], Julio C. Monge [b], Esteban Cañibano [a], Carlos P. Rodriguez-Juan [b], Karina C. Núñez [c,*]

[a] Foundation for Research and Development in Transport and Energy (CIDAUT), Pl. Vicente Aleixandre Campos, 2, 47151 Boecillo, Valladolid, Spain
[b] Ingeniería y Sistemas de Ensayos no Destructivos (ISEND), Parque Tecnológico de Boecillo, Luis Proust, 10, 47151 Boecillo, Valladolid, Spain
[c] Department of Condensed Matter Physics, Faculty of Sciences, University of Valladolid, Paseo de Belén, 7, 47011, Valladolid, Spain

ARTICLE INFO

Keywords:
Non-destructive testing
Eddy current testing
Electrical conductivity
Friction stir welding
Aluminum alloys
Microhardness

ABSTRACT

Constant monitoring of manufacturing processes is crucial for ensuring high-quality products and cost-effectiveness. Non-destructive testing (NDT) techniques, such as eddy current testing (ECT), offer a direct and accurate means of evaluating weld quality in real-time. ECT can assess microstructural changes in welded materials by measuring electrical conductivity. Establishing a robust correlation between electrical conductivity and microstructural changes induced by FSW process parameters remains a critical step to bridge existing knowledge gaps. In this study, electrical conductivity field analysis using eddy currents was conducted on AA6082-T6 FSW joints. A pivotal factor controlling process heat input and influencing defect formation and weld microstructural features is the ratios of FSW tool rotational speed (ω) to travel speed (v). Previous works often evaluated only one set of process parameters, while our study examines multiple combinations of ω and welding speed v to develop a more robust correlation between electrical conductivity and microstructural changes. Both defective and defect-free joints were obtained employing various ω/v ratio and electrical conductivity results were compared with hardness measurements and tensile test results. The analysis reveals a consistent trend between electrical conductivity variations, microstructural changes in weld zones, and microhardness as the ω/ν ratio varies. Our findings show that, at a constant travel speed, an increasing ω/ν ratio is associated with enhanced microhardness and decreased electrical conductivity, attributed to grain refinement. Conversely, at a constant rotational speed, a higher ω/ν ratio leads to increased electrical conductivity, due to the enhanced dissolution of strengthening precipitates. Furthermore, analyzing electrical conductivity profiles and identifying local maxima corresponding to weld failure zones could strengthen the correlation. This approach suggests the potential to assess variations in mechanical properties resulting from process drift, specifically influenced by changes in the ω/v parameter over time. Microstructural analysis through electrical conductivity evaluation emerges as a valuable and predictive tool for assessing weld properties, with promising applications in process monitoring.

1. Introduction

Friction stir welding (FSW) is an outstanding joining technique offering advantages over traditional methods such as tungsten inert gas (TIG) and metal inert gas (MIG) [1]. FSW achieves material joining without the need for melting and subsequent solidification. This solid-state joining process offers numerous advantages, including lower energy input, minimal human intervention, and a more environmentally friendly process due to the absence of welding gases [2]. Additionally, the solid-state nature of FSW addresses the limitations encountered by traditional fusion welding techniques such as solidification cracking and porosity when joining high-strength aluminum alloys [3]. FSW is particularly suitable for dissimilar metal combinations, since FSW operates below the melting point of the base materials minimizing issues related to metallurgical incompatibility [4,5]. This characteristic makes FSW an ideal choice for joining materials with different melting points and thermal expansion coefficients, ensuring superior joint integrity and mechanical properties. Furthermore, FSW reduces distortions and residual stresses while minimizing strength degradation within the weld zone. FSW involves intense mechanical deformation and thermal energy

* Corresponding authors.
E-mail addresses: matmaz@cidaut.es (M. Mazzeschi), karinacarla.nunez@uva.es (K.C. Núñez).

https://doi.org/10.1016/j.jmapro.2024.09.005
Received 3 April 2024; Received in revised form 17 August 2024; Accepted 4 September 2024
Available online 9 September 2024

input, leading to significant changes in the microstructure and properties of the welded material, including grain size refinement, precipitate dissolution, and phase transformations [6]. In particular, heat input plays a critical role in governing defect generation and weld microstructures in FSW. As the primary driving force behind the FSW process, heat input influences the material flow, degree of deformation, and thermal history experienced by the welded components [7]. Variations in heat input can significantly affect the formation of defects. Insufficient heat may hinder material flow and plasticization, leading to the occurrence of defects like tunnel or wormhole defects [8], kissing bonds [9], and lack of fills [1]. Excessive heat levels can induce material softening, resulting in weld nugget collapse, excessive flash formation [10], adhesion of material to FSW tool (surface galling) or anvil (sticking) [11].

Given that FSW is susceptible to defect formation, achieving defect-free FSW joints is imperative, especially in today's manufacturing landscape where delivering high-quality products at minimal costs is essential [12]. In response to this demand, continuous monitoring of manufacturing processes has become crucial [13]. Non-destructive testing (NDT) techniques are instrumental in ensuring the cost-effective operation and safety of industrial components across sectors [14]. Unlike destructive methods, NDT techniques reduce scrap parts, thus lowering product costs. Among various NDT methods applicable to FSW joint quality control, X-radiography [15], ultrasonic testing [16], and eddy current [17] evaluation yield promising results. While X-radiography detects defects causing significant radiation absorption, ultrasonic methods have limitations related to coupling conditions, acoustic attenuation, and defect detectability [18]. Eddy current testing (ECT) has garnered attention for its fast detection, non-contact operation, versatility, and environmental friendliness, making it suitable for real time process monitoring applications and in-field inspections [17].

Real-time process monitoring involves continuously collecting and analyzing data with minimal latency to provide immediate feedback and enable rapid detection and correction of anomalies. Fig. 1 illustrates a typical monitoring architecture for FSW. This architecture focuses on data fusion, where sensor data is aggregated in a "knowledge box" [12]. This fusion integrates experimental data, historical records, and numerical simulations to create a digital twin of the FSW process. The digital twin provides real-time monitoring by combining past data, current observations, and predictive models. It not only tracks the process but also supports decision-making and optimization. When discrepancies arise between real-time data and the digital twin, feedback is sent to the control system to adjust parameters accordingly [19].

The monitoring methods can be traditionally classified into two categories namely, indirect and direct [12]. Indirect means of monitoring sense physical quantities of machines such as current, power, force, torque, vibration etc., Direct methods utilize NDT techniques, including optical, laser and camera vision, to directly assess the quality of produced components by detecting defects.

In the context of FSW, the main indirect methods employed for FSW monitoring used machine signals of vertical and horizontal tool forces [20,21], torque [22,23], and current signals from spindle and feed motors [24]. These methods show good correlation with various weld defects and mechanical properties but rely heavily on trained neural networks, requiring extensive training datasets and specific welding parameters [25].

Common real-time NDT techniques include machine vision [26,27], acoustic emission (AE) [28,29], and phased array ultrasonic testing (PAUT) [30]. These methods are primarily used to detect surface and gap defects and analyze weld regions. The application of digital image processing (DIP) techniques to friction stir welding (FSW) is primarily limited to classifying defective and defect-free welds, with the main limitation being the detection of only surface defects [27]. AE methods detect transient elastic waves from irreversible internal changes in materials, offering valuable insights into welding defects [29]. However, real-time monitoring and control using AE data are challenging due to the high computational demands of processing large data volumes. Kleiner and Bird [30] utilized a PAUT system to evaluate weld quality in 7xxx series aluminum alloys, determining proper forging. PAUT, which uses multiple ultrasonic elements for detailed imaging and inspection, faces challenges such as system complexity and the need for careful selection of scanning parameters like focal distance, inspection angle, and scan pattern, which may require adjustments based on defect location. Upon extensive examination, the authors found no existing studies on the use of ECT for real-time process monitoring of FSW.

Within this framework, ECT offers significant advantages for real-time monitoring due to its non-contact nature, rapid measurement capability, and sensitivity to microstructural changes. In ECT, the electrical conductivity of materials is a crucial parameter due to its direct influence on the electromagnetic response of the inspected component. The high sensitivity of ECT to variations in electrical conductivity, resulting from microstructural changes such as precipitate dissolution or

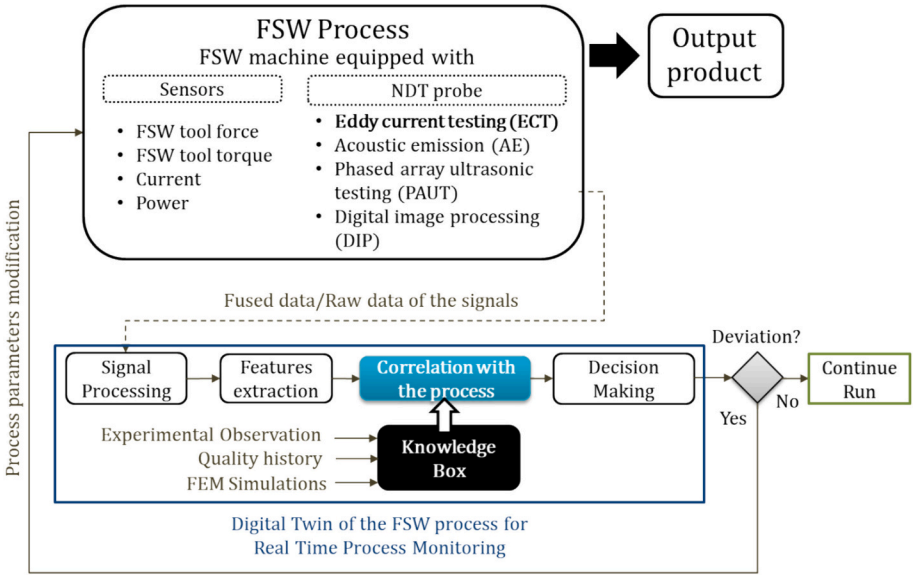

Fig. 1. Schematic representation of real time process monitoring for FSW.
Adapted from [12].

grain refinement, extends beyond mere defect detection. It could facilitate the establishment of a robust correlation between electrical conductivity and the mechanical properties of the weld. This capability has the potential to enhance the development of a more accurate digital twin of the welded joint, improving both the monitoring and predictive capabilities of the welding process. In the context of FSW, the electrical conductivity of the inspected material assumes particular significance due to the substantial modifications it undergoes during the welding process [31]. Assessing the electrical conductivity field provides an indirect method to gauge microstructural alterations within the weld, offering a potential alternative or supplement to hardness assessment [32]. A scaling factor exists between electrical conductivity and microhardness testing due to their mutual dependency on microstructural factors: electrical conductivity reflects electronic mobility, while hardness is influenced by plastic deformation mechanisms like crystal defects, precipitates, and mechanical strengthening [33]. In particular, the electrical conductivity of heat-treatable aluminum alloys, such as those in the 6000 series, is intricately linked to their composition, microstructure, and precipitate distribution. Abdo et al. [34] investigated the influence of alloying elements such as copper and magnesium, as well as thermal and mechanical treatments, on the electrical conductivity of aluminum alloys. Their findings indicate that these factors significantly affect conductivity by altering the microstructure and precipitate distribution. Additionally, Cui et al. [35] demonstrated that the dissolution of precipitates enhances conductivity by reducing electron scattering and thus increasing electron mobility. Coarser grains were found to improve conductivity by minimizing the overall surface area of grain boundaries, which impede electron flow [32,35].

Previous research on ECT in FSW joints has primarily concentrated on detecting a range of common defects, including lack of penetration [36], kissing bonds [16,36], root micro defects [37,38], cavities [36,39], and tunnel defects [36]. These investigations involved developing and validating probes with enhanced sensitivity [39,40], as well as combining ECT with other non-destructive testing methods [16] and implement variations of conventional technique such as Pulsed eddy current (PEC) [41] and Lorentz force eddy current testing (LET) [42].

However, there remains a limited understanding of the relationship between alterations in electrical conductivity and the physical and metallurgical phenomena occurring during both solid-state and fusion-based welding processes. Santos et al. [32] conducted an analysis of electrical conductivity fields to evaluate FSW joints in AA6013 and AA7075 alloys, revealing a consistent correlation between variations in microstructure across the joint's transverse section and changes in both hardness and electrical conductivity. Similarly, in another study [31], profiles of electrical conductivity and hardness in various friction stir processed materials and gas tungsten arc welded AISI 304 stainless steel were compared, consistently demonstrating that an increase in hardness corresponded to a decrease in conductivity within FSW regions. Additionally, Malikov and Ishkov [43] observed variations in average grain size within the microstructure of welded joints, which were directly linked to changes in electrical conductivity. Sorger et al. [31] employed four-point probe and eddy currents testing as non-destructive techniques to investigate microstructural changes in various materials welded by FSW. Their study demonstrated that electrical conductivity provides a more comprehensive understanding of microstructural alterations across a range of materials, including Ti6Al4V, Cu, Pb, S355 steel, and AISI 304 stainless steel. This research highlights a qualitative relationship between electrical conductivity and hardness, offering valuable insights into material properties. To the best of authors' knowledge, no studies have investigated the electrical conductivity of AA6082-T6 aluminum alloy FSW welded joints. AA6082-T6 is notable for its high strength, superior corrosion resistance, and excellent machinability, making it a favored material in numerous engineering applications [44]. It possesses the highest strength among the 6000 series alloys, with tensile strength 10 % to 18 % higher than that of Aluminum 6061, depending on thickness [45]. Additionally, its overall corrosion resistance is enhanced due to a lower copper content compared to Al-6061. The alloy's exceptional strength-to-weight ratio is particularly beneficial in the aerospace and automotive industries, where reducing weight without sacrificing structural integrity is paramount.

This study investigates the electrical conductivity of various AA6082 FSW joints produced under different process parameters to achieve both defective and defect-free joints by altering the heat input.

Previous works have typically evaluated only a single set of process parameters, whereas our study investigates multiple combinations of rotational speed (ω) and welding speed (v), providing a comprehensive analysis of how changes in heat input affect electrical conductivity. Specifically, we conducted a comparative analysis of electrical conductivity fields, microhardness evaluations, and mechanical properties across various ratios of FSW tool rotational speed (ω) to travel speed (v). This critical parameter not only influences defect formation and weld microstructural features in FSW joints but its variation over time could represent potential process drifts during manufacturing. The ultimate goal is to leverage electrical conductivity field analysis as a valuable tool for evaluating weld properties, including defects and mechanical characteristics with a potential application in monitoring process stability.

2. Experimental procedure

2.1. Materials, processing and characterization

The material under investigation was a 6082-T6 aluminum alloy under the form of rolled plates of 3 mm thickness. Yield strength, ultimate tensile strength, and elastic modulus of the base material were determined following ISO 6892-1 standards. These mechanical properties were measured using an MTS QTEST 159 Universal Testing Machine under controlled temperature and humidity conditions (23 ± 2 °C and 50 ± 10 % RH). Additionally, Vickers microhardness was assessed for the base material with a Buehler 1600/3600 hardness testing machine. Tables 1 and 2 provide detailed information on chemical composition and mechanical properties of the base material. Plates were welded perpendicularly to the rolling direction using a vertical milling machine specific for FSW (Fig. 2). Initially, the plates were securely positioned within the fixture to facilitate the friction stir welding process, as depicted in Fig. 2(a). A tool with an 11.5 mm shoulder diameter and a conical threaded pin with a diameter of 5 mm and a length of 2.7 mm was utilized.

The selection of process parameters was undertaken deliberately to induce the formation of weld seams exhibiting both the presence and absence of defects. A prevalent flaw encountered in FSW is the occurrence of wormholes, a continuous void situated completely inside the weld region along the length of the weld, eluding detection by human operators [49]. Due to the decreased joint area between parts, wormholes pose a significant threat, substantially compromising the mechanical integrity of the weld. There are indications suggesting that the ω/v / ratio plays a significant role in influencing the formation of the wormhole defect [49]. Crawford et al. [50] observed that for $\omega/v < 1.3$ rev/min^{-1} a wormhole is likely to develop in AA6061-T6 FSW butt joints. Kim et al. reported [51] wormhole defect occurring for ω/v values between 1 and 5 rev/min^{-1} and for different values of plunge down force in 4 mm ADC12 FSW welded plates. Salih et al. developed a thermo-mechanical finite element model for simulating the FSW process of aluminum alloy AA 6082-T6. Experimental and numerical findings demonstrated that employing a ω/v ratio of 4 (with ω = 800 rpm and v = 200 mm/min) led to inadequate and uneven plastic deformation during welding, resulting in decreased flow of softened metal behind the tool and subsequent formation of wormhole defect.

Based on the previous considerations, the process parameters were defined to encompass a spectrum of values for parameter ω/v, ensuring the fabrication of welded joints both with and without wormhole defects. Table 3 summarizes the employed welding parameters.

Tensile test specimens were extracted from each weld in accordance

Table 1
Chemical compositions in % of 6082 aluminum alloy [46].

Si	Fe	Cu	Mn	Mg	Cr	Zn	Ti	Al
0.7–1.3	Max 0.5	0.1	0.4–1.0	0.6–1.2	Max 0.25	Max 0.2	Max 0.1	Rest

Table 2
Properties of the base metal AA6082-T6.

Yield strength (MPa)	Ultimate tensile strength, UTS (MPa)	Elastic modulus, E (GPa)	Microhardness [HV]	Electrical conductivity [% IACS] [47]	$T_{melting}$ (°C) [48]
310	355	67	118.1	44	650

with ISO 25239-4, having dimension of 50 mm gauge length and 12.5 mm width. Tensile tests were under controlled temperature and humidity conditions, maintained within the range of 23 ± 2 °C and 50 ± 10 % RH, respectively.

Vickers microhardness measurements were conducted employing a Buehler 1600/3600 hardness testing machine. Measurements were taken along the length of the specimens with 0.3 mm between consecutive indentations, positioned at a distance of 0.8 mm from the upper surface, corresponding to the point of entry for the FSW tool. The evaluation of Vickers microhardness serves as a valuable tool in distinguishing variations attributable to changes in grain size, defect content, and precipitate distribution across the distinct weld zones, namely the stirred zone (SZ), thermo-mechanically affected zone (TMAZ), and heat-affected zone (HAZ) [1]. The SZ undergoes dynamic recrystallization and texture formation due to frictional heat and intense plastic deformation, influenced by tool rotational speed and traverse speed. Adjacent to the SZ is the TMAZ, characterized by reduced strains, strain rates, and peak temperatures compared to the SZ [1]. This region typically exhibits grain distortion patterns indicative of material shearing and flow around the rotating tool. Lastly, the HAZ encompasses both sides of the SZ, experiencing primarily thermal effects without significant plastic deformation. The thermal diffusivity, as well as electrical and thermal conductivities, are crucial factors in the development of the nugget zone during FSW. These properties influence the heat distribution and peak temperatures achieved during the welding process, which are fundamental in forming a robust nugget zone. The significance of these parameters in the context of FSW is discussed in the work by Serier et al. [52], which highlights their impact on the thermal profile and weld quality.

In order to detect weld defects within the inner zone of the welded joint, X-ray radiography inspections were also conducted on FSW joints. These inspections also served as an NDT approach, complementing the interpretation of results obtained through eddy current testing. X-ray radiography inspections were performed employing a cathode tube potential of 100 kV and a beam current of 0.25 mA, with an exposure time of 1300 ms. The resulting X-ray images were subjected to post-processing using Image J software, which included appropriate light-dark contrast grading to enhance visualization and analysis of internal structures and defects within the specimens.

2.2. Eddy currents testing

Eddy current testing (ECT) utilizes electromagnetic induction by passing alternating current through a coil to produce a varying magnetic field. When placed near a conductive material, such as metal, this field induces eddy currents within the material. These currents generate magnetic fields that interact with the original field, allowing detection and analysis of material defects or conductivity variations through changes in impedance or electromagnetic properties. The depth of penetration is a critical parameter in eddy current testing, delineating the extent to which the electromagnetic field permeates the material. The depth of penetration (δ) is defined as the depth below the surface of

Table 3
Process parameters used for each welded specimen.

Sample code	Tool rotational speed, ω [rpm]	Travel speed, v [mm/min]	ω/v [rev/mm]
w1	600	600	1.0
w2	1200	900	1.3
w3	1200	700	1.7
w4	400	200	2.0
w5	600	200	3.0
w6	800	200	4.0
w7	1200	300	4.0
w8	1200	200	6.0
w9	1000	120	8.3
w10	1000	90	11.1
w11	1200	90	13.3
w12	1000	60	16.7

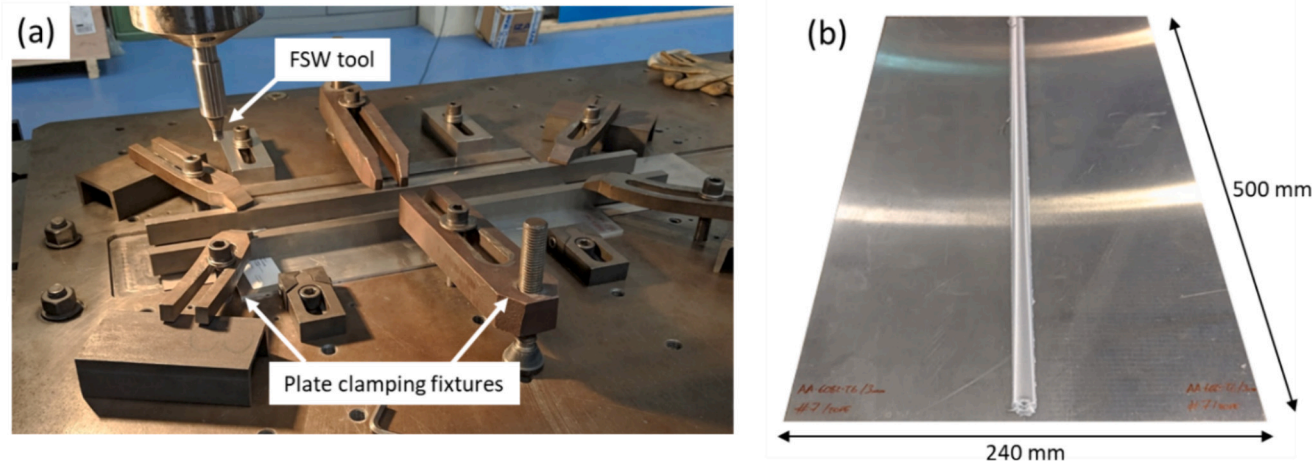

Fig. 2. (a) Bench of the vertical milling machine used for friction stir welding, FSW tool and plate clamping fixtures. (b) Image of one of the manufactured butt joints.

the conductor at which the current density has fallen to 36.79 % of the material surface density [32]. This depth is determined by various factors, including the frequency of the alternating current (f), magnetic permeability (μ), and electrical conductivity of the material (σ) and it could be expressed by the following equation [32]:

$$\delta = \frac{1}{\sqrt{\pi f \mu \sigma}} \quad (1)$$

In the presence of discontinuities, defects, or microstructural alterations, variations in the local electrical conductivity and magnetic permeability of the material occur, facilitating the detection of microstructural features. Higher frequencies yield shallower penetration depths, making them more sensitive to surface defects, while lower frequencies enable deeper penetration, suitable for detecting subsurface anomalies.

Electrical conductivity measurements were performed using an absolute cylindrical helicoidally probe with a 10 mm diameter and with a ferrite core of 2 mm diameter,1230 turns of the coil and permanent lift-off of 0.5 mm (Fig. 3), with signal generation and acquisition conducted using DEFdiscover® platform (ISEND S.A.).

The electrical conductivity at each point in the material was determined from the real and imaginary components of the probe's electrical impedance. The impedance measurement incorporates factors such as electrical conductivity, probe lift-off, frequency, and magnetic permeability. In non-ferromagnetic materials, the magnetic permeability remains constant, thus the impedance is primarily influenced by electrical conductivity, lift-off, and frequency. With lift-off and frequency held constant throughout all measurements, variations in electrical impedance directly corresponded to changes in electrical conductivity. The procedure began with the calibration of the ECT equipment using AA6082-T6 standard reference materials with known conductivity values to ensure accuracy. The FSW specimens were then subjected to ECT by positioning the absolute eddy current probe in close proximity to the weld surface, maintaining consistent probe orientation and spacing for all measurements. The resulting impedance changes were meticulously recorded and analyzed, facilitating a detailed mapping of the electrical conductivity distribution across the weld zone. The 5 MHz frequency was selected to ensure a penetration depth of up to 1.5 mm into the material. The inspections were conducted perpendicular to the weld seam, as depicted in Fig. 4(a), on both the upper and lower surfaces relative to the FSW tool entry point, with the spacing between lines set at 30 mm. The extreme zones of the weld seam having an extension of 40 mm were excluded from inspection due to transient phenomena occurring in these areas, which may not accurately reflect the actual process parameters set in the machine.

Assessments on the upper surface aimed to evaluate conductivity alterations attributed to varied microstructural characteristics within the weld, while inspections on the lower surface targeted the identification of the wormhole defect. In the upper surface inspections, the excitation frequency was chosen to accurately assess conductivity measurements within the weld area, specifically targeting the region where microhardness values were obtained (Fig. 4(b)), in order to investigate the correlation between electrical conductivity and weld microhardness. In contrast, during the inspection of the lower face, the frequency was strategically chosen to concentrate the eddy currents subsuperficially. This decision was made to enable the identification of the wormhole defect with heightened sensitivity (Fig. 4(c)).

3. Result and discussion

3.1. X-ray inspection results

The X-ray inspections reveal the existence of a wormhole defect in six of the twelve manufactured samples as reported in Table 4. The genesis of such defect lies in the anomalous flow of material due to insufficient heat provided during the welding process. Insufficient thermal input during the process can arise from various factors, including the combination of low rotational speed (ω) and high travel speed (v) values. In fact, wormhole defect was found for exactly the lowest ω/v ratio values. In these cases, insufficient heat is generated due to limited contact duration between the workpiece and the tool, impeding the effective softening and blending of the material with a consequent inadequate plastic deformation. Notably, there is a transition zone around a ω/v ratio of approximately 4, where conditions shift from defective to defect-free. This transition is governed by critical values of ω and v, which determine the heat input. As detailed in Section 3.2, each constant ω/v ratio has a specific threshold of ω or v that marks the boundary between the presence and absence of defects. Fig. 5(a) and (b) shows the typical appearances of X-ray radiographies for a welded joint respectively without defect and with the presence of a wormhole defect. For all cases considered, the defect was found in the bottom of the weld at a distance of approximately 0.5 mm from the lower surface of the samples as shown in Fig. 5(d) by taking a lateral cross section of the weld. The positioning of the wormhole can be attributed to the insufficient material flow in the bottom of the weld, as evidenced by previous studies on flow patterns during the FSW process [53,54]. Consequently, the diminished material flow coupled with inadequate plasticity due to insufficient heat input, leads to the formation of the defect in this region of the weld. Of particular interest is the welded sample w1 (Fig. 6), which shows an area along the weld seam where X-ray analysis reveals the presence of the wormhole defect alongside defect-free regions. Furthermore, the X-ray examination indicates a gradual size increase of the defect as it extends from the defect-free section towards the FSW tool exit. A potential reason for the selective occurrence of the wormhole defect in only one extension of the weld seam could be variations in local mechanical stresses or thermal gradients during the welding process. For example, uneven distribution of residual stresses or temperature gradients along the weld path may create preferential zones for defect formation. Additionally, factors such as local variations in material flow dynamics, including turbulence or irregularities in tool movement, could contribute to the formation of defects in specific regions of the weld.

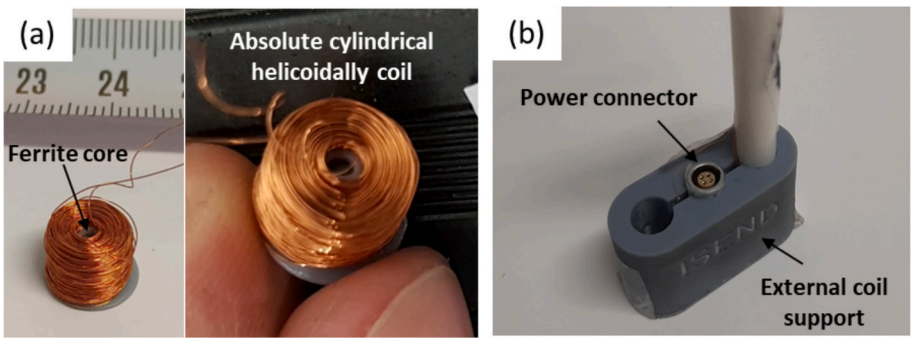

Fig. 3. (a) Absolute cylindrical helicoidal probe used for conductivity measurements. (b) External support structure and power connector.

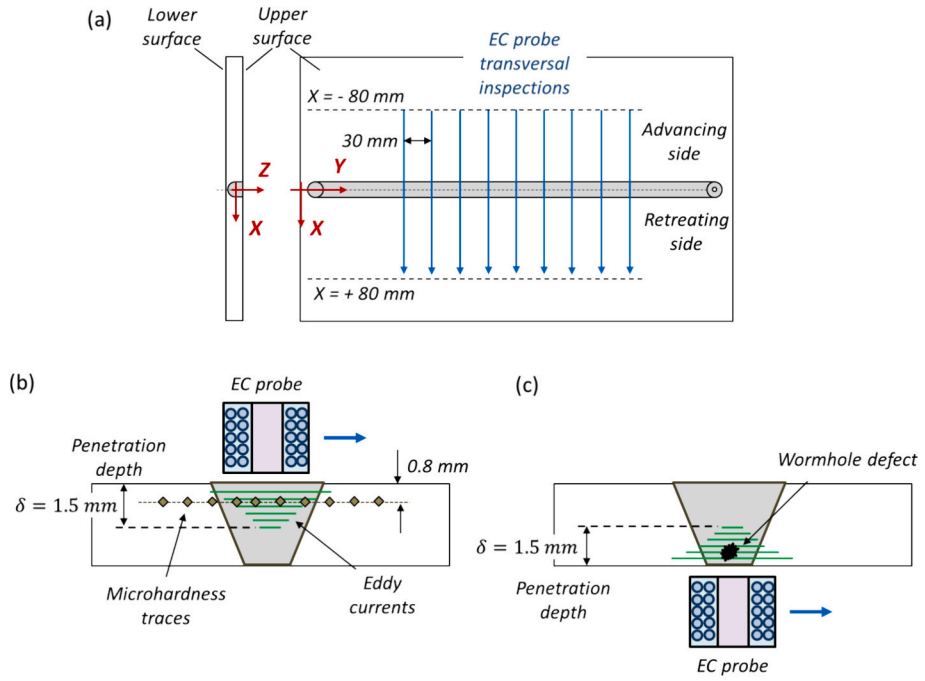

Fig. 4. (a) Movements of the eddy current probe in a transversal FSW inspection. (b) Upper surface assessments evaluating conductivity changes due to microstructural variations. (c) Lower surface inspections identifying wormhole defects.

Table 4
Results of X-ray inspections to identify the presence of defects in the welded joints considered.

Sample code	ω/v	X-ray results
w1	1.0	Wormhole defect
w2	1.3	Wormhole defect
w3	1.7	Wormhole defect
w4	2.0	Wormhole defect
w5	3.0	Wormhole defect
w6	4.0	Wormhole defect
w7	4.0	No defects
w8	6.0	No defects
w9	8.3	No defects
w10	11.1	No defects
w11	13.3	No defects
w12	16.7	No defects

Nevertheless, this particular sample provided an excellent opportunity to assess the probe's capability in detecting the defect and observing local variations in electrical conductivity along the weld seam.

3.2. Tensile tests and microhardness measurements

Stress-strain curves of base material and the welded samples are given respectively in Fig. 7(a), (b) and (c), whereas Table 5 presents the tensile properties, joint efficiency and microhardness values for base material and FSW specimens.

Compared to the base material, FSW specimens show a reduction in tensile values expressed by a joint efficiency between 62 and 70 % for no defective joints and between 53 and 62 % for defective joints (Table 5). The degradation in mechanical properties stems from the nature of heat-treatable Al-alloys, such as AA6082-T6, wherein strengthening mechanisms rely on the formation of second-phase precipitates to enhance strength. During FSW process, the temperature in the nugget zone elevates to 400–550 °C due to friction between the tool and workpiece, alongside plastic deformation surrounding the rotating tool. This elevated temperature prompts degradation in the base metal, including precipitate dissolution and coarsening, within and around the SZ of FSW joints resulting in weakened joint integrity [55]. This is the reason why a decrease in hardness within the nugget zone and tensile properties of the welded sample respect to the base material is observed as reported in Table 5 due to the disruption of the artificial ageing T6 treatment (obtained at approximately 180 °C [56]). Furthermore, considering the welded samples from w1 to w6, the presence of a wormhole defect impacts tensile properties, evidenced by decreased ultimate tensile stress (UTS) values and significant reductions in elongation, as illustrated by the pronounced drop in the strain-stress engineering curves for the defective welds depicted in Fig. 7(b) The exhibited brittle nature of the defective specimens could be attributed to the creation of stress concentration points within the weld region by the presence of a wormhole defect. Previous studies [57–59] have shown that welding defects can lead to fatigue cracks due to stress concentration. These defects amplify stress at the defect site during tensile testing, causing premature failure and a more abrupt decrease in stress. Furthermore, the structural irregularities caused by the wormhole defect can initiate crack propagation and structural instability within the weld zone, exacerbating the drop in stress and resulting in a more pronounced deviation from the stress-strain behavior of defect-free samples.

In evaluating the microhardness values and tensile properties of the welded samples across different process parameters investigated in this study, it is essential to consider two key phenomena within the weld: the intensity of heat input and the degree of deformation.

Arbegast and Hartley [60] proposed a pseudo-heat index (ω^2/ν) to characterize the relationship between welding parameters and heat generation. It has been demonstrated that, for numerous aluminum alloys, a generalized correlation between FSW parameters and maximum temperature (T) can be described using Eq. (2) [60].

$$\frac{T}{T_m} = K\left(\frac{\omega^2}{\nu \cdot 10^4}\right)^{\alpha} \tag{2}$$

where the exponent α varies between 0.04 and 0.06, and the constant K between 0.65 and 0.75. T_m, in °C, is the melting point of the alloy.

Fig. 8 illustrates the process window where specific combinations of ω-v pairs tested in the study are categorized based on weld quality outcomes—whether defects were present or absent. The plot features

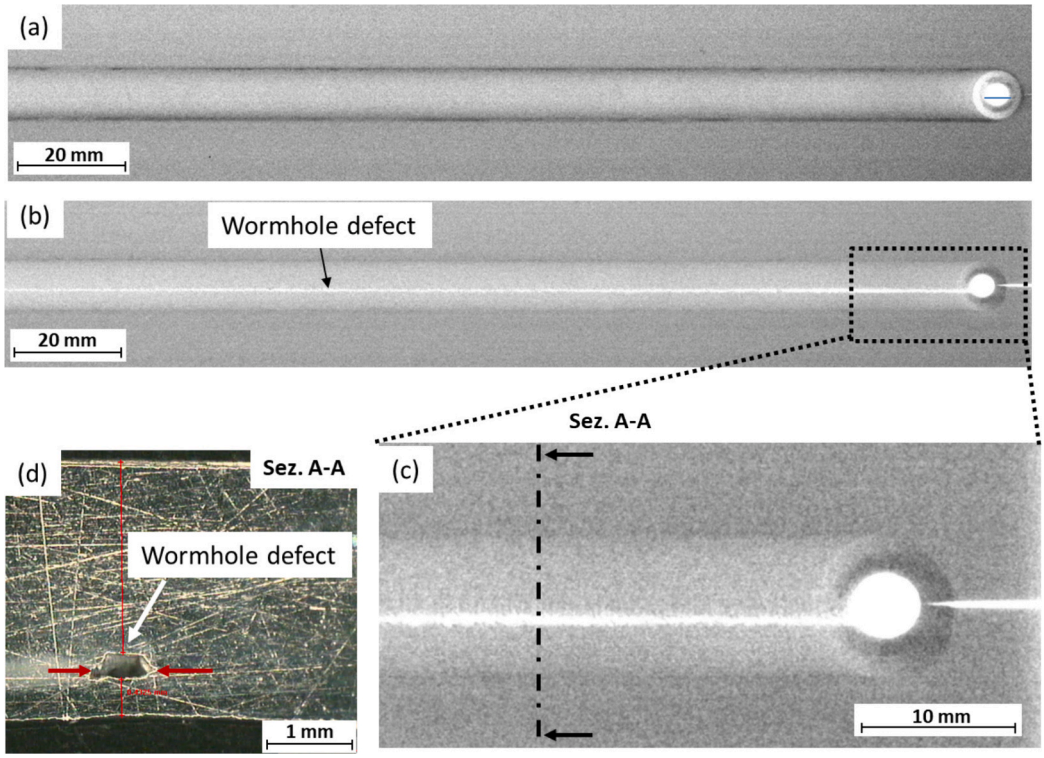

Fig. 5. Frontal X-ray inspection showing a welded joint (a) without defect (w9) and (b) with wormhole defect (w4). (c) Magnification at the FSW tool exit hole and (d) cross section of the wormhole defect obtained by microscopic analysis.

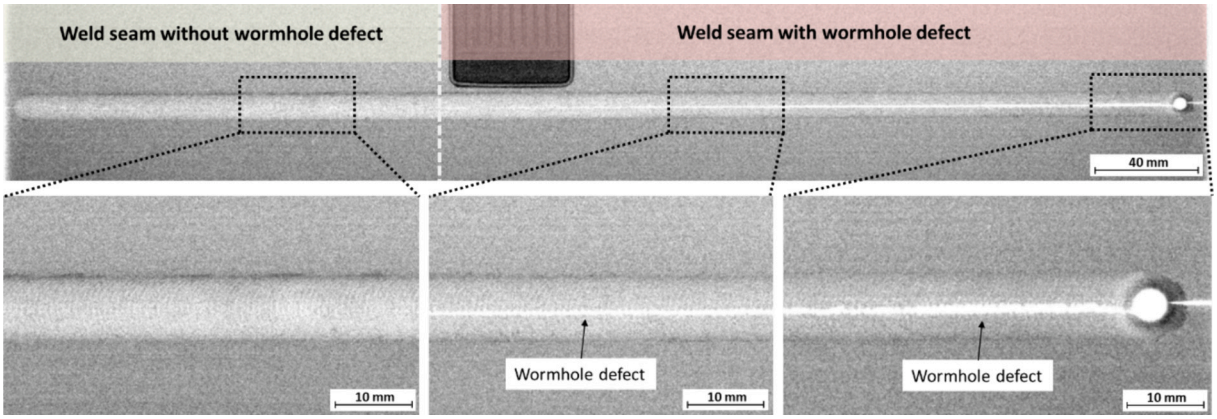

Fig. 6. Frontal X-ray inspection of the welded joint w1 showing a section of the weld seam with and without the wormhole defect.

contour lines representing constant temperature levels, derived using Eq. (2), which delineate areas within the process window where heat input remains consistent despite variations in ω and v settings. These contours provide visual insights into how temperature distribution influences defect formation in friction stir welding (FSW) joints. According to the findings of this study, a critical cut-off temperature ($T_{cut-off} = 407^{\circ}C$) is identified, below which insufficient heat input predominates, leading to an increased likelihood of wormhole defect formation. This threshold is clearly depicted in figure, aiding in the identification of process parameter combinations that promote defect formation.

Additionally, the plot includes straight contour lines representing constant ω/v ratio values, which traverse the process window and illustrate how variations in ω and v impact weld quality at fixed ratios. Contours corresponding to lower ω/v ratios exhibit a shallow slope, indicating consistent insufficient heat input across the parameter space and consequently higher incidences of wormhole defects. As the ω/v ratio increases, the contours traverse transition zones where defect occurrence varies.

An illustrative case highlighted in Fig. 8 is observed at ω/v = 4 (welds w6 and w7), which serves as an example illustrating the general trend observed across the dataset. Welds produced at this ratio demonstrate a transition zone where defect occurrence is sensitive to both ω and v values individually, emphasizing their combined influence rather than the ratio alone.

Fig. 9 shows the variation of UTS and microhardness in the nugget zone as the ω/v ratio varies considering for each case the maximum input temperature estimated with Eq. (2). The results are organized by varying the ω/v parameter while keeping one of the two process variables constant. Specifically, three levels of constant rotational speed (600, 1000, 1200 rpm) and a scenario with constant welding speed (200 mm/min) were considered, as illustrated in Fig. 8. The cases at a constant rotational speed of 1200 rpm and a constant welding speed of 200

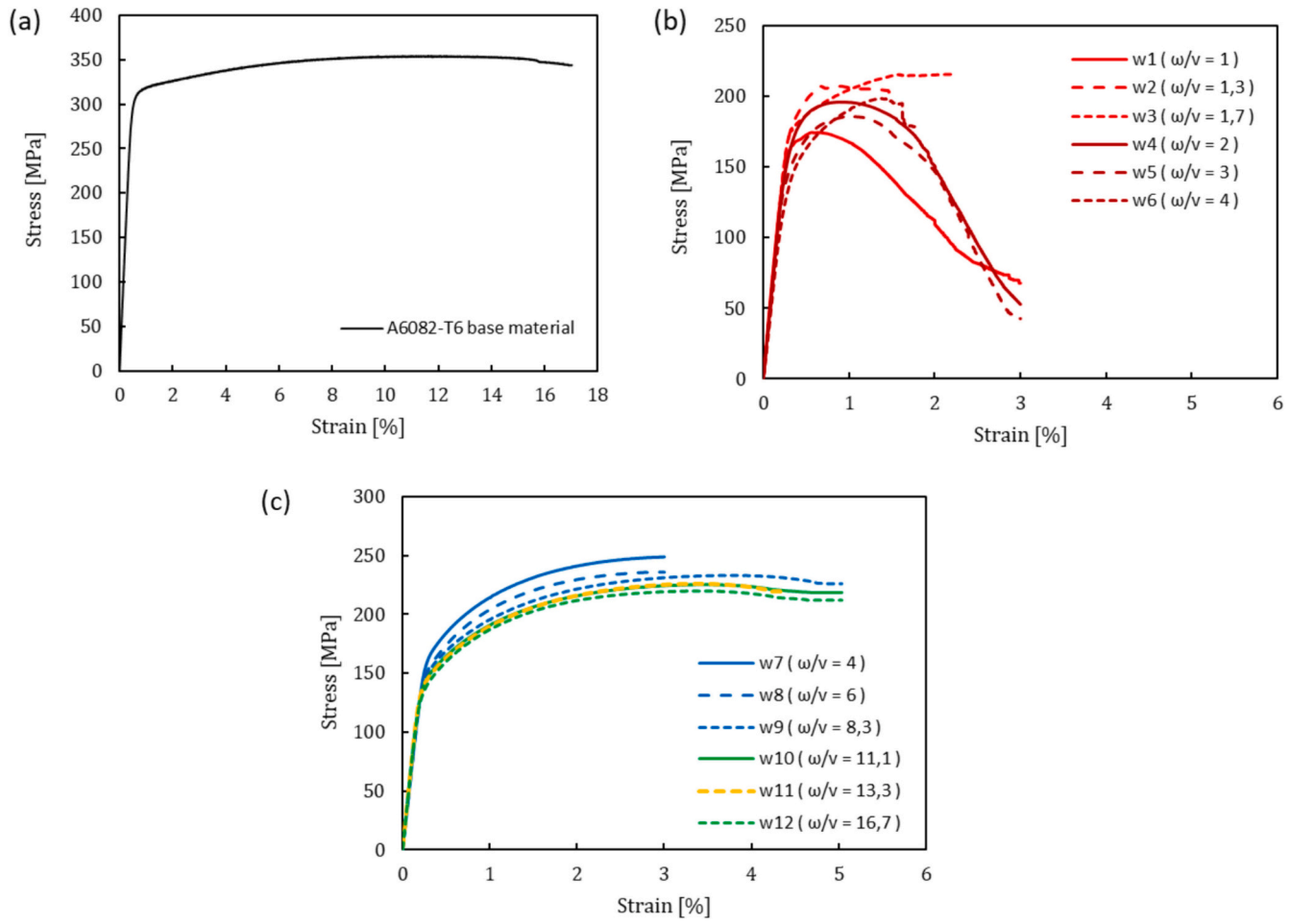

Fig. 7. Engineering stress–strain curves for (a) AA6082-T6 base material, (b) defective and (c) no defective FSW joints.

Table 5
Tensile properties and microhardness results for FSW welded specimens and AA6082-T6 base material.

Sample code	UTS [MPa]	Joint efficiency [%]	Microhardness[a] [HV]
Base 6082-T6	355.0	–	118.1
w1	188.0	53 %	65.6
w2	210.0	59 %	92.7
w3	221.0	62 %	93.3
w4	198.0	56 %	71.7
w5	186.4	53 %	61.4
w6	207.6	58 %	64.0
w7	249.4	70 %	90.4
w8	236.3	67 %	87.0
w9	233.5	66 %	94.0
w10	226.0	64 %	81.7
w11	226.2	64 %	82.8
w12	220.2	62 %	84.5

[a] Evaluated in the Stir Zone (between $x = -2$ mm and $x = +2$ mm) for welded specimens.

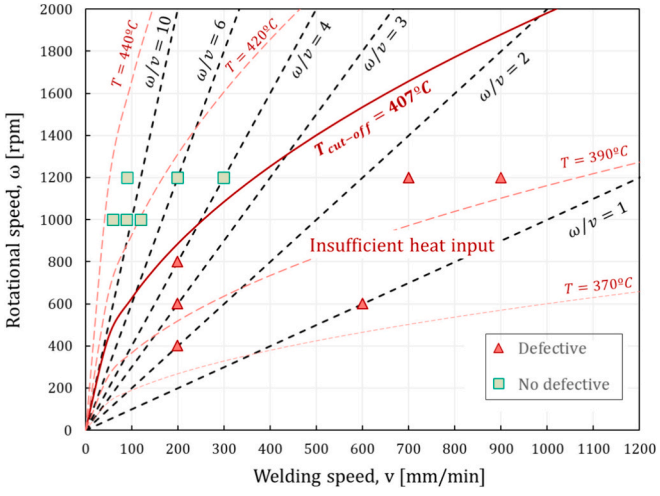

Fig. 8. Process window highlighting the relationship between process parameters, heat input, and defect occurrence based on the specific combinations of ω-v pair tested in the present study.

mm/min are of particular interest as they intersect the defect-to-non-defect transition zone.

Low values of the ω/v ratio result in reduced frictional heating, leading to inadequate material flow and the formation of weld defects such as wormholes, as previously discussed. In Fig. 9(a), as the heat input increases with rising rotational speed, a threshold rotational speed of approximately 886 rpm is identified. This threshold marks the transition from the presence to the absence of the wormhole defect. The limited degree of deformation fails to induce sufficient grain refinement, as evidenced by the notably lower microhardness values observed in defective welds; conversely, increasing the rotational speed enhances grain refinement, resulting in higher microhardness values in defect-free welds. The observed inverse relationship between microhardness and grain size can be attributed to the higher density of grain boundaries in

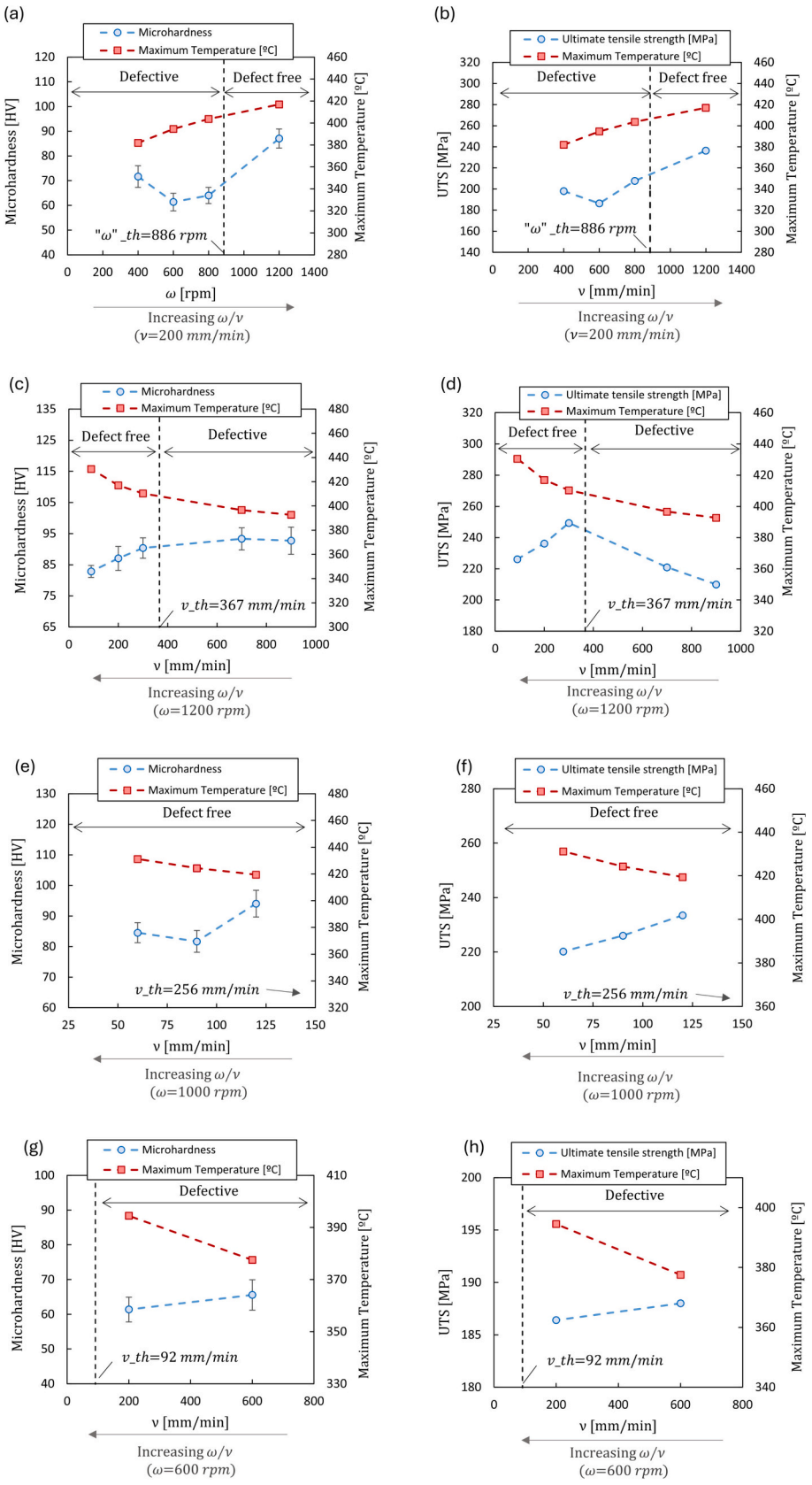

Fig. 9. Variation of maximum input temperature, UTS, and microhardness values in the SZ as the ω/ν ratio changes. Panels (a) and (b) illustrate the impact of varying rotational speed at a constant welding speed of 200 mm/min. Panels (c) and (d) show the effects of varying welding speed at a constant rotational speed of 1200 rpm, (e) and (f) at 1000 rpm, and (g) and (h) at 600 rpm.

refined grain structures. This increased density impedes dislocation movement, enhancing the material's resistance to plastic deformation and consequently leading to higher microhardness values. Conversely, coarse grain structures are associated with lower microhardness values due to fewer grain boundaries and increased susceptibility to plastic deformation. A similar trend is observed in the UTS values shown in Fig. 9(b). Moving from defective samples to free-defect w8 weld, an increase in UTS from an average value of 193 MPa to 236 MPa is clearly observable. This relevant change is likely attributed to intense frictional heating and plastic deformation within the stir zone associated with the higher values of ω/ν ratio resulting in fine-grained microstructure.

When considering the scenario where the rotational speed is kept constant while varying the welding speed, a reduction in welding speed results in an increase in the ω/ν ratio, thereby leading to a higher heat input. As depicted in Fig. 9(c) this adjustment is associated with a decrease in microhardness values as the heat input increases, observable from right to left across the graph. This decline may be attributed to the simultaneous increase in both the degree of deformation and the heat input. Elevated frictional heating could result in extensive growth of recrystallized grains within and around the stirred zone, alongside the dissolution of strengthening precipitates. This aspect is also evident in the UTS values within the defect-free zone (Fig. 9(d)), where a further increase in the ω/ν ratio results in a slight decrease in UTS, attributed to the dissolution of strengthening precipitates. For defective joints, although the hardness values are high, approximately 93 HV and higher than in defect-free joints, the presence of the wormhole defect significantly reduces the load-bearing section and acts as a stress concentrator, leading to diminished mechanical performance.

Among the welds examined in this study, the most favorable balance between the degree of deformation and heat input was achieved with welded sample w7, exhibiting a UTS of 249.4 MPa. In the remaining cases where rotational speed is held constant while welding speed is varied (Fig. 9(e)–(h)), there is a consistent trend of decreasing microhardness and UTS with increasing heat input across the range of welding speeds investigated. In these cases, as the ω/v ratio increases, the dissolution of precipitates emerges as the predominant factor influencing the observed trends, despite the concurrent increase in the degree of deformation.

Figs. 10 and 11 show the specimen after tensile tests respectively for defective and free-defect FSW welds. For joints with defects (w1-w6), failure occurred within the weld nugget (SZ, Fig. 10(g)), primarily attributed to lower microhardness values observed in these specimens, likely exacerbated by the presence of wormholes, which facilitated nucleation and propagation of the failure. Fig. 12(a) depicts hardness

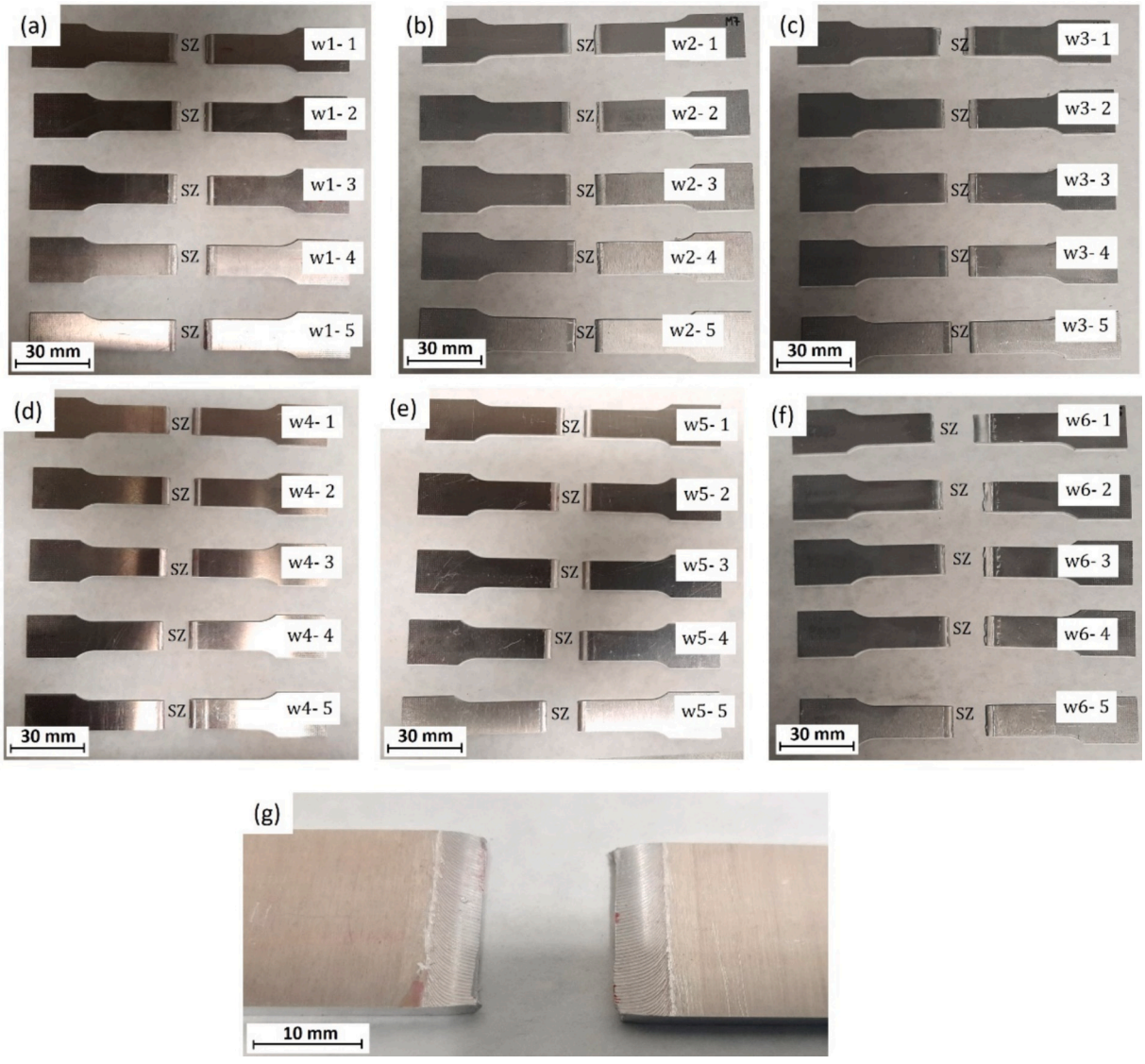

Fig. 10. (a)–(f) Defective FSW joints after test. (g) A detailed view of the rupture zone in correspondence of SZ observed within these specimens.

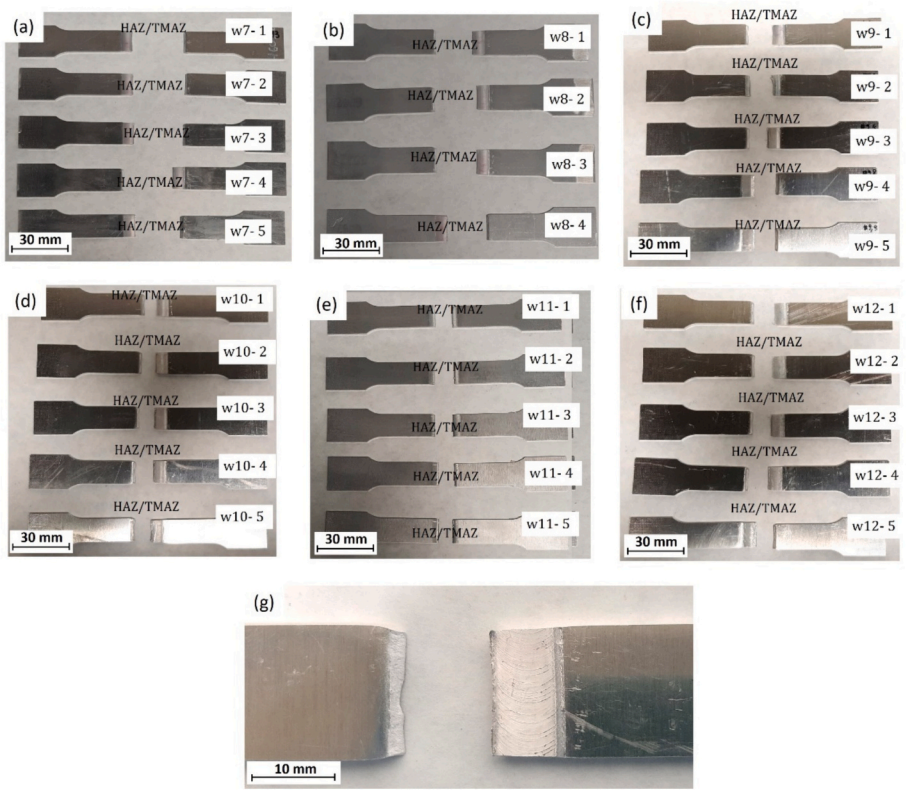

Fig. 11. (a)–(f) No defective FSW joints after test. (g) A detailed view of the rupture zone in correspondence of transition zone between TMAZ and HAZ observed within these specimens.

profiles for defective joints, revealing a V-shaped pattern with minimum microhardness observed at the central region of the weld nugget. For defect-free welds (w7-w12), fracture occurred outside the welded area, as depicted in Fig. 11. In these joints, microhardness values within the SZ exhibit higher levels. The increased heat input, which typically induces grain refinement within the SZ, also suggests a potential for grain coarsening within the HAZ zone. Specifically, Fig. 12(b) illustrates microhardness profiles with a W-shaped pattern, indicating a minimum at the HAZ/TMAZ transition zone. The HAZ undergoes thermal cycling during welding and generally exhibits lower microhardness values compared to other regions.

3.3. Eddy currents testing results

The electrical conductivity of heat-treatable Al-alloys is influenced by composition, defects, microstructure, and precipitate distribution. Alloying elements like copper and magnesium affect conductivity [34] and thermal and mechanical treatments also alter conductivity by modifying microstructure and precipitate distribution [47]. Coarser grains enhance the electrical conductivity. Indeed, the overall surface

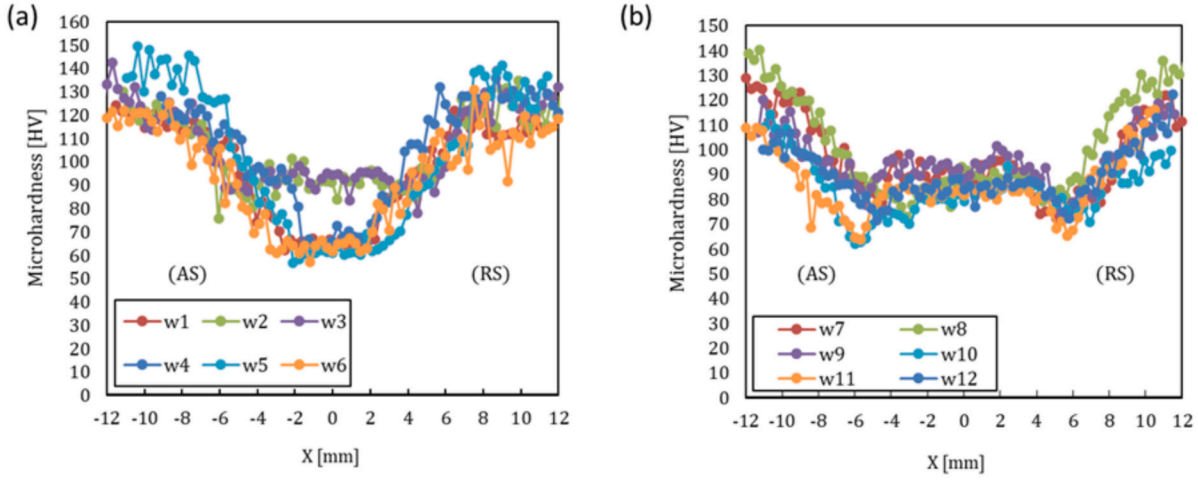

Fig. 12. Vickers hardness profile in (a) defective and (b) defect free FSW joints.

area of grain boundaries per unit volume opposes electron mobility and its reduction promotes an increment of electrical conductivity [32]. The dissolution of precipitates in 6000 series aluminum alloys typically results in an increase in electrical conductivity [35,61]. This occurs because the dissolution of precipitates reduces the scattering of electrons within the material, allowing for greater electron mobility and therefore higher conductivity.

In this study, with a single material type under investigation, the alterations in electrical conductivity are primarily driven by variations in grain size, defects, and precipitate dissolution, highlighting these as the primary influencing variables.

Fig. 13 illustrates the changes in microhardness values and electrical conductivity within the SZ as the ω/ν ratio varies, as observed through eddy current inspection conducted on both the upper and lower surfaces of the welded joint. As done previously, the results are organized by varying the ω/v parameter while maintaining one of the two process variables constant. Specifically, three levels of constant rotational speed (600, 1000, 1200 rpm) and a scenario with constant welding speed (200 mm/min) were considered.

Comparison of microhardness values and electrical conductivity on the upper surface reveals a reciprocal trend with varying ω/ν ratio for all cases considered. Electrical conductivity, influenced by electron mobility, and microhardness, indicative of material resistance to plastic deformation primarily governed by dislocations and grain size, demonstrate an inverse relationship, a trend also observed by other researchers across various welded aluminum alloys and process parameters [32,33,43,62]. As the ω/ν ratio changes, enhancements in microhardness attributed to grain refinement align with reductions in electrical conductivity.

As illustrated in Fig. 13(a), the elevated microhardness values previously observed in defect-free joints correspond to the lowest electrical conductivity values measured on the upper surface. In contrast, as shown in Fig. 13(b), (c) and (d), a decrease in weld speed (increasing ω/ν ratios) leads to increased electrical conductivity. This increase in conductivity can be attributed to the enhanced dissolution of strengthening precipitates, which plays a more influential role compared to other factors. This phenomenon occurs alongside previously discussed reductions in microhardness, underscoring the complex interplay between thermal inputs and microstructural changes.

In examining the conductivity values obtained from the lower surface, it is noteworthy that in defective welds, these values are lower than those measured on the upper surface. Conversely, for defect-free welds, the lower surface conductivity values exceed those of the upper surface. The presence of the wormhole, acting as a void within the material, results in a localized reduction in electrical conductivity. This accounts for the observed decrease when comparing the conductivity curves between the upper and lower surface of the weld.

Conversely, in the absence of defects, the electrical conductivities on the lower side exhibit higher values compared to the upper side, likely attributed to the smaller extent of the SZ on the lower face of the weld.

The Fig. 14 illustrates the electrical conductivity variation in welded joint w1, the weld sample showing, according to the radiographic evidence, regions without defects and areas with progressively larger wormholes along the weld seam. Notably, measurements on the lower side exhibit steady values in defect-free regions, but a gradual decrease in conductivity with the appearance of the wormhole. Conversely,

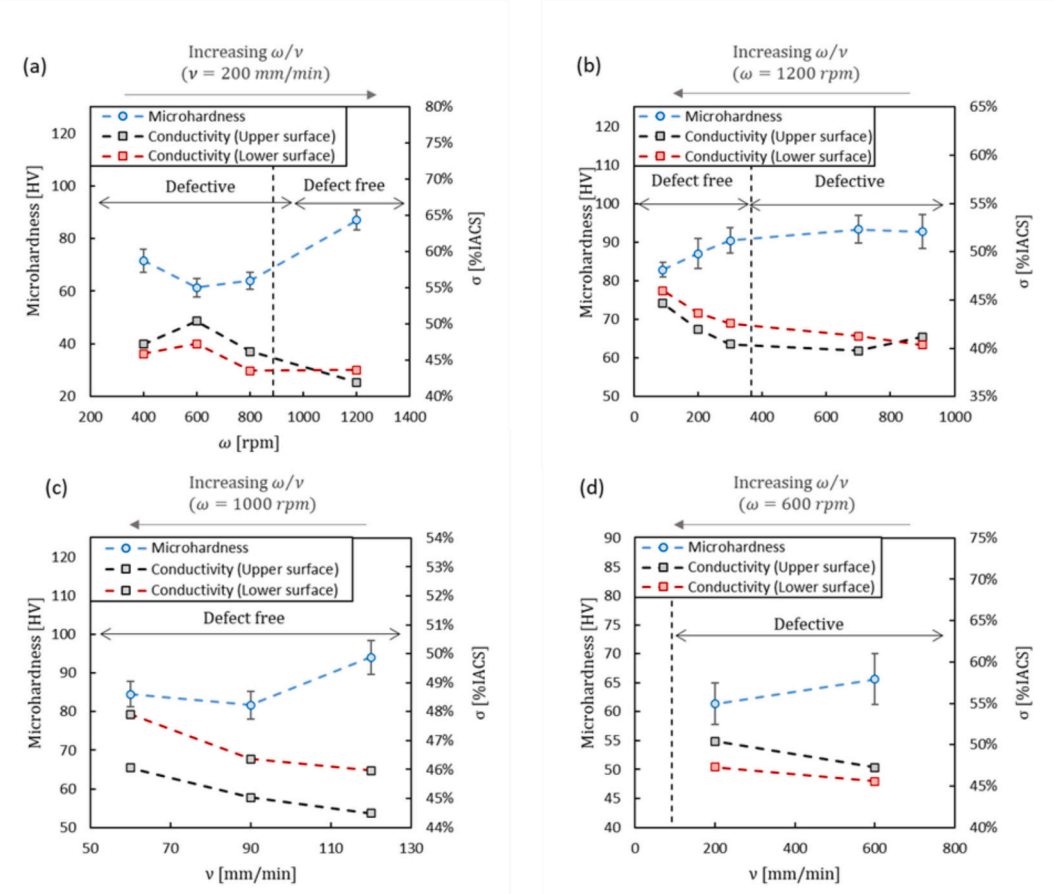

Fig. 13. Variation of the microhardness values and electrical conductivity in SZ as the ω/ν ratio changes. Panel (a) illustrates the impact of varying rotational speed at a constant welding speed of 200 mm/min. Panel (b) shows the effects of varying welding speed at a constant rotational speed of 1200 rpm, and (c) at 1000 rpm, and (d) at 600 rpm. Conductivity values were obtained by performing eddy current inspection in both the upper and lower face of the welded joint.

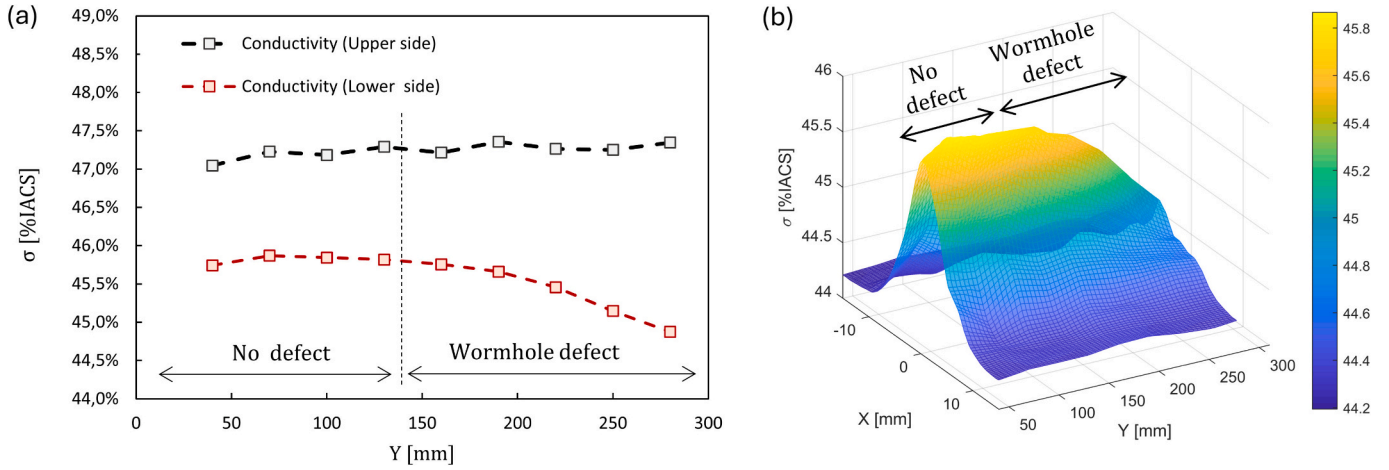

Fig. 14. (a) Variation of electrical conductivity in the SZ along the weld seam (X = 0) evaluated in both the upper and lower face of the w1 FSW welded joint. (b) Tridimensional representation of the electrical conductivity evaluated in the lower face of the w1 FSW welded joint along X and Y directions.

measurements on the upper surface remain relatively constant, indicating limited penetration of eddy currents without any interaction with the defect. This result affirms the distinct purposes of the two measurements: those on the upper side aim to characterize microstructural influences such as grain size and precipitates on electrical conductivity, whereas measurements on the lower surface are oriented towards defect detection. However, the difference in conductivity between defective and defect-free regions in the range of 100–200 mm is minimal, posing challenges for using ECT to distinguish between these conditions effectively, as shown in Fig. 14. This limitation underscores the necessity of addressing the detectability threshold of ECT in identifying such defects. The subtle variations in conductivity indicate that while ECT is adept at detecting changes in microstructural properties, its effectiveness in defect detection may be limited by the resolution of the existing probe configuration. Enhancing defect detectability may require optimizing the probe design. Adjustments in parameters such as frequency, lift-off distance, and coil configuration could significantly improve the sensitivity of ECT to subtle variations in electrical conductivity.

Fig. 15 depicts measured values of electrical conductivities in a tridimensional imaging evaluated on the upper side in X-Y direction. Samples welded at a constant speed of 200 mm/min while varying the rotational speed were represented in Fig. 15. Notably, the w1 sample was included, demonstrating a similar conductivity profile. The Fig. 15 (f) shows electrical conductivity profiles with respect to the center of the weld obtained as average values along the weld seam. In the first three cases examined having the lowest values of ω/ν ratio, the electrical conductivity distribution exhibits a bell-shaped profile, increasing from the base material and peaking at the center of the weld nugget. Given the inverse correlation between microhardness and electrical conductivity, this is exactly the opposite shape of V-shaped hardness profile observed in Fig. 12(a), with a minimum value at the center of the SZ. This aspect was also supported by the fracture patterns observed in Fig. 10, where all specimens exhibited fractures in the center of the weld. As the ω/ν ratio increases, there is a noticeable expansion in the cross-sectional area of the weld bead exhibiting alterations in electrical conductivity compared to the base material. While ratios of 1 and 2 show a consistent width of approximately 15 mm with similar conductivity changes, a more pronounced expansion occurs at ratio 3, spanning about 20 mm. This phenomenon correlates with the heightened heat input accompanying an increase in the ω/ν ratio. This elevated heat input prompts increased dissolution of precipitates and coarsening of grains within the TMAZ and HAZ, consequently augmenting electron mobility. Fig. 15(d) illustrates the conductivity distribution for a joint located near the transition zone between defective and defect-free states. This distribution begins to exhibit a transformation towards the characteristic "W" shape observed in defect-free joints, as shown in Fig. 15(e).

In the scenario of constant rotational speed (1200 rpm) with varying welding speed, as depicted in Fig. 16, the two cases with wormhole defects exhibit a V-shaped profile, reflecting a decline in electrical conductivity within the stir zone (SZ). This inversion of electrical conductivity, when compared to the earlier cases (w1, w4, and w5), is associated with higher hardness in the welded nugget, indicative of greater grain refinement. The welded joint w7, situated in the transition zone, also displays a similar profile. Here, a slight increase in conductivity within the nugget zone becomes more evident with increasing heat input ($\omega/v = 6$ in Fig. 14(e)), eventually forming the W shape characteristic of defect-free joints at high ω/ν ratios.

Considering higher heat input, Fig. 17 exhibits the three-dimensional mapping of electrical conductivities for w9, w10, and w12 samples, characterized by constant rotational speed of 1000 rpm. In this scenario, W-shape electrical conductivity shapes is predominant for ω/ν ratios of 8.3 and 11.1, and a pronounced asymmetric profile with elevated values on the advancing side for the maximum ω/ν ratio of 16.7 is observed. Furthermore, an expansion in the cross-sectional area of the weld seam by approximately 25 mm, displaying variations in electrical conductivity, is noted due to the increased heat input. The W-shaped electrical conductivity profile observed can be attributed to more significant dissolution of precipitates and grain coarsening in TMAZ and HAZ. Consequently, there is an increase in electron mobility within these regions, resulting in higher electrical conductivity. Upon closer examination of the conductivity profile across the weld seam, it becomes apparent that the highest conductivity values are not situated at the center of the weld, but rather at the boundary between the HAZ and TMAZ. The localization of conductivity maxima elucidates why all w9, w10, and w12 samples failed at the transition zone between TMAZ and HAZ, as depicted in Fig. 11. Indeed, peak conductivity corresponds to minimal microhardness, as clearly observed considering the microhardness profiles in Fig. 12. Regarding the w12 sample, the asymmetric profile of the electrical conductivity can be attributed to the uneven distribution of heat and plastic deformation during welding. The advancing side experiences higher heat input and greater plastic deformation compared to the retreating side, leading to differences in microstructural evolution [63]. This can result in variations in grain size, precipitate distribution, and defect formation, all of which influence electrical conductivity.

Additionally, the flow of material during welding may not be uniform, causing variations in the distribution of alloying elements and microstructural features, such as a larger size of the HAZ in the advancing side [7]. These factors combined contribute to the asymmetric profile observed in the advancing side of the w12 sample,

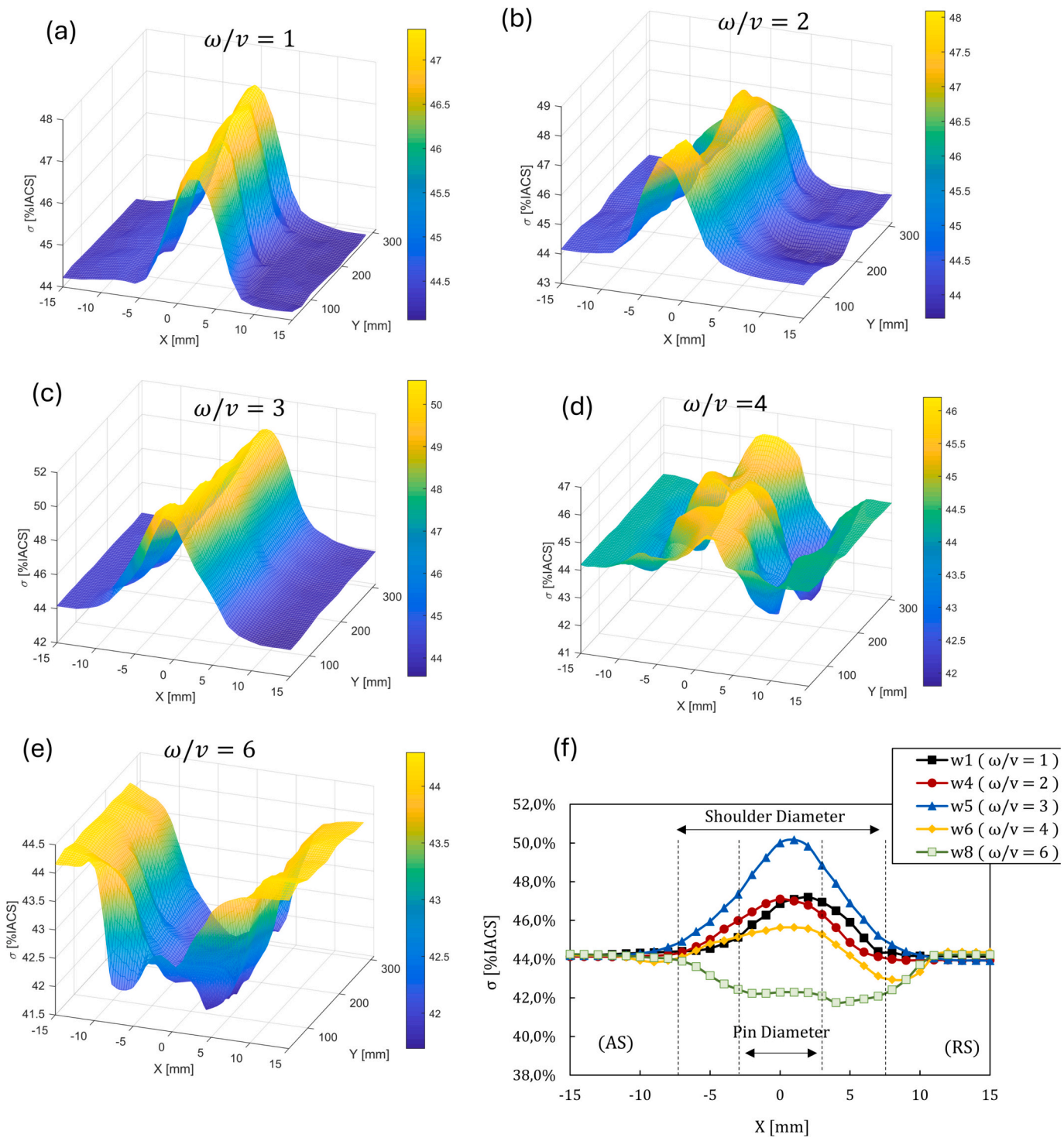

Fig. 15. Tridimensional representation of the electrical conductivity evaluated in the upper face along X and Y directions. Electrical conductivity maps of FSW joints obtained at a constant welding speed of 200 mm/min while varying the rotational speed were represented: (a) w1, (b) w4, (c) w5, (d) w6, (e) w8. w1 sample was included, demonstrating a similar conductivity profile. (d) Electrical conductivity profile obtained by taking average values along Y direction.

characterized by the highest heat input.

Fig. 18 illustrates the correlation between microhardness, UTS, and electrical conductivity, based on the data obtained in this study. Measured data points alongside linear interpolation curves are represented, offering a clear visual representation of the relationships among these critical parameters.

Fig. 18(a) demonstrates an inverse correlation between microhardness and electrical conductivity, suggesting that changes in microstructural properties, such as grain refinement and precipitate dissolution, significantly impact both properties. This correlation underscores the potential of using electrical conductivity as a non-destructive proxy for assessing microhardness variations across welded joints. Similarly, Fig. 18(b) shows an inverse relationship between UTS and electrical conductivity. This finding supports the feasibility of using electrical conductivity measurements to predict UTS, facilitating the prognosis of mechanical performance without resorting to destructive

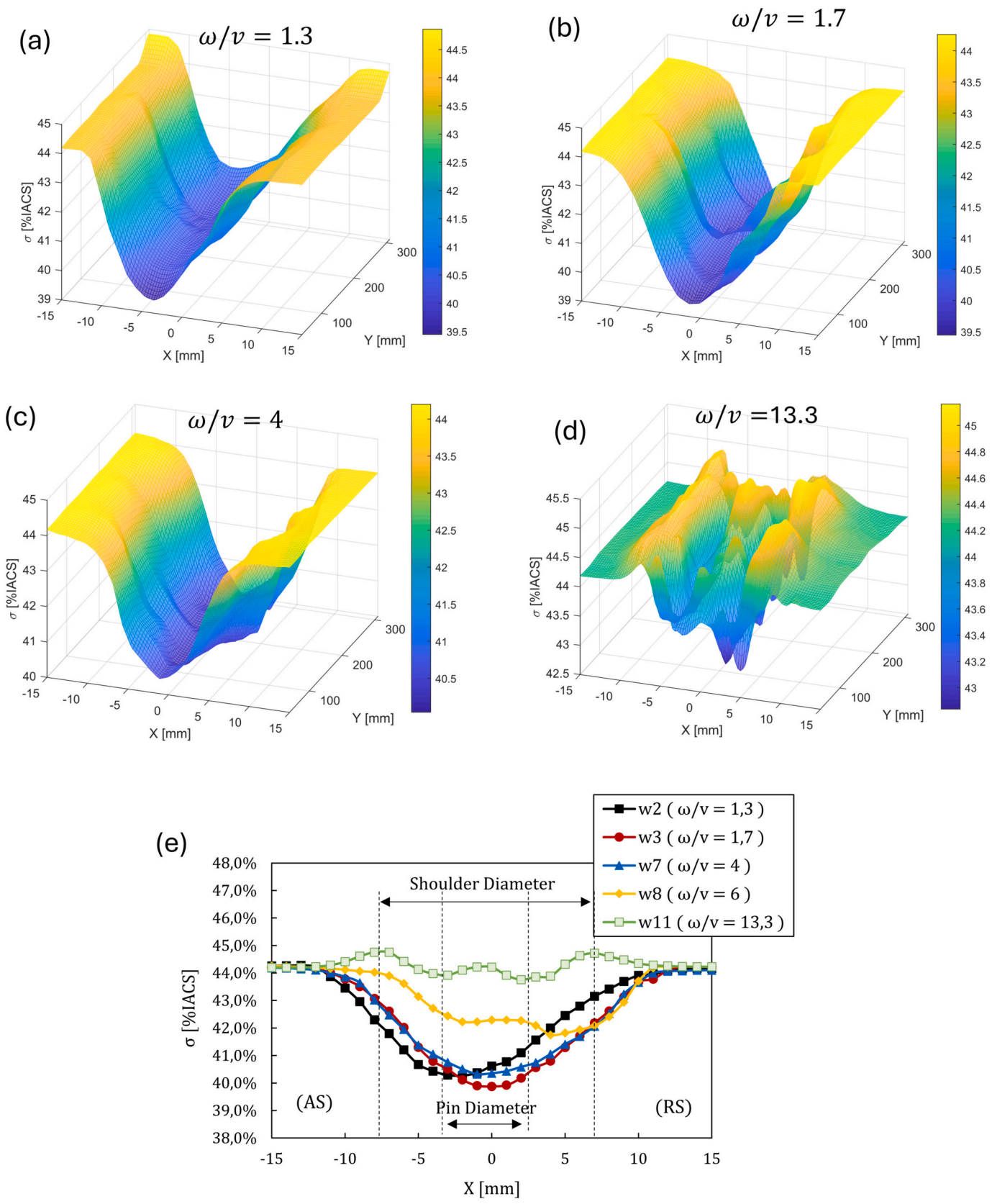

Fig. 16. Tridimensional representation of the electrical conductivity evaluated in the upper face along X and Y directions. Electrical conductivity maps of FSW joints obtained at a constant rotational speed of 1200 rpm while varying the welding speed were represented: (a) w2, (b) w3, (c) w7, (d) w11. (e) Electrical conductivity profile obtained by taking average values along Y direction.

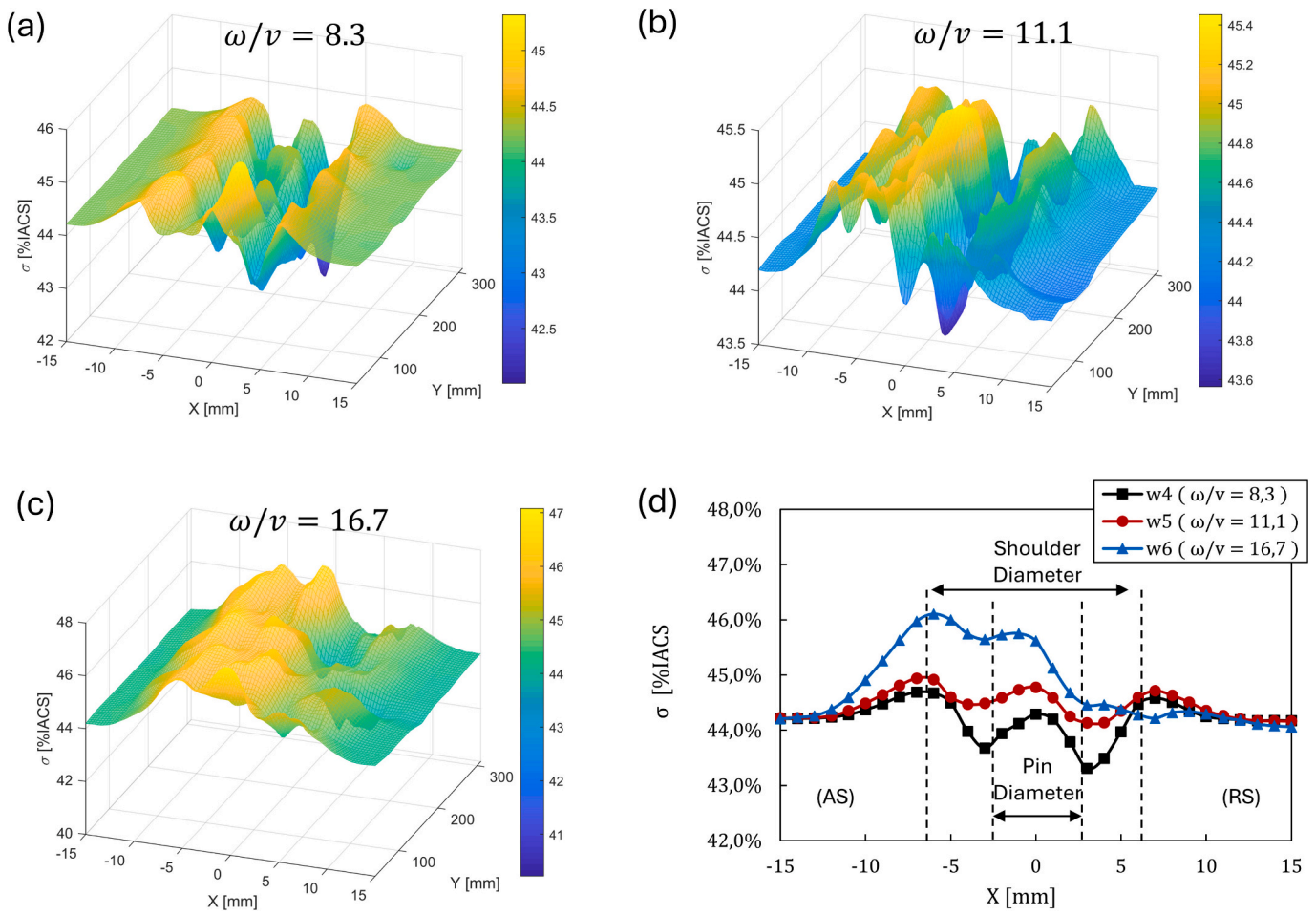

Fig. 17. Tridimensional representation of the electrical conductivity evaluated in the upper face along X and Y directions. Electrical conductivity maps of FSW joints obtained at a constant rotational speed of 1000 rpm while varying the welding speed were represented: (a) w9, (b) w10, (c) w12. (d) Electrical conductivity profile obtained by taking average values along Y direction.

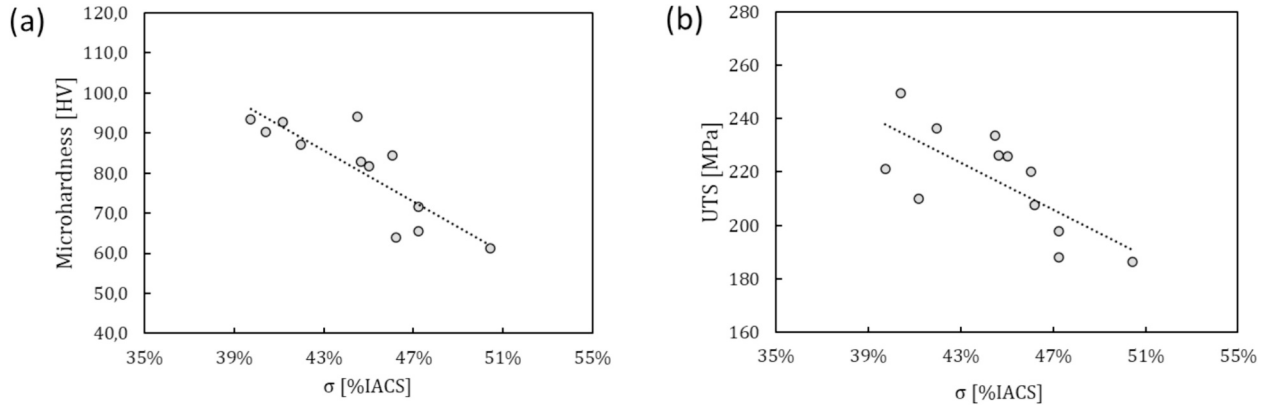

Fig. 18. Correlation between (a) microhardness, (b) UTS, and electrical conductivity.

testing.

However, it is crucial to obtain calibration curves with a high confidence level, which requires thorough testing with a larger number of specimens. Further experimentation and validation using diverse specimen sets would enhance the robustness and reliability of the relationship between electrical conductivity measurements and joint integrity.

4. Conclusions

By adjusting the ω/v ratio, both defective and defect-free FSW joints were successfully fabricated.

Subsequent electrical conductivity field analysis using eddy currents was performed for each joint, with results compared to microhardness analysis, x-ray inspection, and tensile test outcomes. The main conclusions of the present study are as follows:

(1) Substantial modifications in the electrical conductivity of welded materials are evident across all examined samples as a result of FSW.
(2) Changes in electrical conductivity reflect microstructural alterations across different zones of the weld revealing a reciprocal trend with microhardness values as the ω/v ratio varies.
(3) An expansion in the cross-sectional area of the weld seam from 15 mm to approximately 25 mm, displaying variations in electrical conductivity, is observed as the heat input (ω/v ratio) increases.
(4) FSW joints, whether exhibiting wormholes or located near the transition zone between defective and non-defective regions, display a bell-shaped or V-shaped conductivity distribution.
(5) For almost all defect-free joints analyzed in this study, electrical conductivity exhibits a W-shaped distribution. The maximum peak values of electrical conductivity measurements correspond to the location of the failure zone in the weld where minimum values of microhardnesss are expected.
(6) The integration of the obtained correlations between electrical conductivity and weld properties into the welding process monitoring framework could offer a robust approach for real-time prognosis of weld properties. Electrical conductivity assessment has the potential to detect any process drifts induced by microstructural variations, enabling timely interventions to maintain weld quality.

In conclusion, our study emphasizes the significant influence of the ω/v ratio on defect formation and demonstrates the effectiveness of electrical conductivity analysis in evaluating the resulting microstructural changes to control potential process drift. However, our investigation only covers a specific range of process variables. To validate our findings and explore broader trends, we recommend further studies with varying combinations of tool rotational speed and transverse speed. Additionally, future research should focus on dissimilar materials FSW joints, examining how electrical conductivity varies between different materials. Moreover, exploring the impact of temperature on conductivity for real-time process monitoring applications holds promise for enhancing process control and ensuring weld quality across various industrial settings. Recent advancements in dynamic signal analysis provide critical insights into temperature-conductivity relationships, aiming to mitigate the impact of material temperature, as highlighted in the work of Xia et al. [64]. These developments hold significant promise for enhancing the effectiveness of real-time monitoring. These investigations not only have the potential to enhance the reliability of friction stir welding but also paves the way for advanced predictive maintenance strategies, ultimately improving the overall efficiency and quality of the welding process.

CRediT authorship contribution statement

Mattia Mazzeschi: Writing – original draft, Validation, Methodology, Investigation, Formal analysis, Data curation, Conceptualization. **Miguel Sanz:** Writing – review & editing, Validation, Investigation, Formal analysis, Data curation. **Julio C. Monge:** Methodology, Investigation, Formal analysis, Data curation, Conceptualization. **Esteban Cañibano:** Writing – review & editing, Supervision, Methodology, Formal analysis. **Carlos P. Rodriguez-Juan:** Writing – review & editing, Validation, Methodology, Formal analysis, Conceptualization. **Karina C. Núñez:** Writing – review & editing, Supervision, Resources, Project administration, Funding acquisition, Formal analysis, Conceptualization.

Declaration of competing interest

The authors declare that they have no known competing financial interests or personal relationships that could have appeared to influence the work reported in this paper.

Acknowledgments

The authors would like to thank the Recovery and Resilience Mechanism Funds - New Generation EU Funds and the Community of Castilla y León Funds. Complementary Research and Development Plans with the Autonomous Communities in R&D&I actions, under Component 17. Investment 1. “Materiales Avanzados Con Funcionalidades Avanzadas Para La Nueva Transformación Tecnológica”. Authors also acknowledges the University of Valladolid for the Postdoctoral Contract CONVOCATORIA 2020 (K.C.N.C)

References

[1] Mishra RS, Ma ZY. Friction stir welding and processing. Mater Sci Eng R Reports 2005;50(1–2):1–78. https://doi.org/10.1016/j.mser.2005.07.001.
[2] Jain R, et al. In: Davim JP, editor. Friction stir welding: Scope and recent development BT-modern manufacturing engineering. Cham: Springer International Publishing; 2015. p. 179–229. https://doi.org/10.1007/978-3-319-20152-8_6.
[3] Çam G, Mistikoglu S. Recent developments in friction stir welding of al-alloys. J. Mater. Eng. Perform. 2014;23(6):1936–53. https://doi.org/10.1007/s11665-014-0968-x.
[4] Guo Z, Ma T, Yang X, Li J, Li W, Vairis A. Multi-scale analyses of phase transformation mechanisms and hardness in linear friction welded Ti17(α + β)/Ti17(β) dissimilar titanium alloy joint. Chinese J Aeronaut 2024;37(1):312–24. https://doi.org/10.1016/j.cja.2023.08.018.
[5] Guo Z, et al. In-situ investigation on dislocation slip concentrated fracture mechanism of linear friction welded dissimilar Ti17(α+β)/Ti17(β) titanium alloy joint. Mater Sci Eng A 2023;872(February). https://doi.org/10.1016/j.msea.2023.144991.
[6] Salih OS, Ou H, Sun W. Heat generation, plastic deformation and residual stresses in friction stir welding of aluminium alloy. Int J Mech Sci 2023;238, no. October: 107827. https://doi.org/10.1016/j.ijmecsci.2022.107827.
[7] Laska A, Sadeghi B, Sadeghian B, Taherizadeh A, Szkodo M, Cavaliere P. Temperature evolution, material flow, and resulting mechanical properties as a function of tool geometry during friction stir welding of AA6082. J Mater Eng Perform 2023;32(23):10655–68. https://doi.org/10.1007/s11665-023-08671-1.
[8] Zhao Y, Zhou L, Wang Q, Yan K, Zou J. Defects and tensile properties of 6013 aluminum alloy T-joints by friction stir welding. Mater Des 2014;57:146–55. https://doi.org/10.1016/j.matdes.2013.12.021.
[9] Zhou N, Song D, Qi W, Li X, Zou J, Attallah MM. Influence of the kissing bond on the mechanical properties and fracture behaviour of AA5083-H112 friction stir welds. Mater Sci Eng A 2018;719(February):12–20. https://doi.org/10.1016/j.msea.2018.02.011.
[10] Ahmadi H, Arab NBM, Ghasemi FA, Farsani RE. Influence of pin profile on quality of friction stir lap welds in carbon Fiber reinforced polypropylene composite. Int J Mech Appl 2012;2(3):24–8. https://doi.org/10.5923/j.mechanics.20120203.01.
[11] Podržaj P, Jerman B, Klobčar D. Welding defects at friction stir welding. Metalurgija 2015;54(2):387–9.
[12] Mishra D, Roy RB, Dutta S, Pal SK, Chakravarty D. A review on sensor based monitoring and control of friction stir welding process and a roadmap to industry 4.0. J Manuf Process 2018;36(November):373–97. https://doi.org/10.1016/j.jmapro.2018.10.016.
[13] Li CJ. In: Wang L, Gao RX, editors. Signal processing in manufacturing monitoring BT - condition monitoring and control for intelligent manufacturing. London: Springer London; 2006. p. 245–65. https://doi.org/10.1007/1-84628-269-1_10.
[14] Kumar S, Vishwakarma M, Akhilesh P. Advances and researches on non destructive testing: a review. Mater. Today Proc. 2018;5(2):3690–8. https://doi.org/10.1016/j.matpr.2017.11.620.
[15] F. Cosmi, A. Cristofori, L. Mancini, R. Tovo, G. Tromba, and M. Volpone, “5450 - PRELIMINARY INVESTIGATION BY SYNCHROTRON RADIATION OF CRACKS AND DEFECTS IN AA FSW SAMPLES,” 2013. [Online]. Available: https://api.semanticscholar.org/CorpusID:137371198.
[16] A. Lamarre, O. Dupuis, and M. Moles, “Complete inspection of friction stir welds in aluminum using ultrasonic and eddy current arrays,” *ASM Proc.* Int Conf Trends Weld Res, vol. 2005, pp. 219–225, 2005.
[17] Gao P, Wang C, Li Y, Cong Z. Electromagnetic and eddy current NDT in weld inspection: a review. Insight Non-Destructive Test. Cond. Monit. 2015;57(6):337–45. https://doi.org/10.1784/insi.2015.57.6.337.
[18] Rosado LS, Santos TG, Piedade M, Ramos PM, Vilaça P. Advanced technique for non-destructive testing of friction stir welding of metals. Meas. J. Int. Meas. Confed. 2010;43(8):1021–30. https://doi.org/10.1016/j.measurement.2010.02.006.
[19] Liu M, Fang S, Dong H, Xu C. Review of digital twin about concepts, technologies, and industrial applications. J Manuf Syst 2021;58(June):346–61. https://doi.org/10.1016/j.jmsy.2020.06.017.
[20] Boldsaikhan E, Corwin EM, Logar AM, Arbegast WJ. The use of neural network and discrete Fourier transform for real-time evaluation of friction stir welding. Appl Soft Comput J 2011;11(8):4839–46. https://doi.org/10.1016/j.asoc.2011.06.017.

[21] Al-Sabur R, Jassim AK, Messele E. Real-time monitoring applied to optimize friction stir spot welding joint for AA1230 Al-alloys. Mater. Today Proc. 2021;42 (2021):2018–24. https://doi.org/10.1016/j.matpr.2020.12.253.
[22] Kumari S, et al. Defect identification in friction stir welding using continuous wavelet transform. J Intell Manuf 2019;30(2):483–94. https://doi.org/10.1007/s10845-016-1259-1.
[23] Das B, Pal S, Bag S. Design and development of force and torque measurement setup for real time monitoring of friction stir welding process. Meas J Int Meas Confed 2017;103:186–98. https://doi.org/10.1016/j.measurement.2017.02.034.
[24] Das B, Pal S, Bag S. Weld quality prediction in friction stir welding using wavelet analysis. Int J Adv Manuf Technol 2017;89(1–4):711–25. https://doi.org/10.1007/s00170-016-9140-0.
[25] Hunt, Johnathon, Larsen, Brigham, and Hovanski, Yuri, "In Line Nondestructive Testing for Sheet Metal Friction Stir Welding," in *WCX SAE World Congress Experience*, SAE International, 2023. doi:https://doi.org/10.4271/2023-01-0069.
[26] Bhat NN, Kumari K, Dutta S, Pal SK, Pal S. Friction stir weld classification by applying wavelet analysis and support vector machine on weld surface images. J. Manuf. Process. 2015;20:274–81. https://doi.org/10.1016/j.jmapro.2015.07.002.
[27] Ranjan R, et al. Classification and identification of surface defects in friction stir welding: an image processing approach. J. Manuf. Process. 2016;22:237–53. https://doi.org/10.1016/j.jmapro.2016.03.009.
[28] Jiménez-Macías E, Sánchez-Roca A, Carvajal-Fals H, Blanco-Fernández J, Martínez-Cámara E. Wavelets application in prediction of friction stir welding parameters of alloy joints from vibroacoustic ANN-based model. Abstr Appl Anal 2014;2014. https://doi.org/10.1155/2014/728564.
[29] S. Kannaiyan, S. Murugesan, D. Thirumalaikannan, B. Visvalingam, and B. P. Nagasai, "Characteristics analysis and monitoring of friction stir welded dissimilar AA5083/AA6061-T6 using acoustic emission technique," Weld Int, vol. 38, no. 8, pp. 556–573, Aug. 2024, doi:https://doi.org/10.1080/09507116.2024.2376187.
[30] Kleiner D, Bird CR. Signal processing for quality assurance in friction stir welds. Insight Non-Destructive Test Cond Monit 2004;46(2):85–7. https://doi.org/10.1784/insi.46.2.85.55545.
[31] Sorger GL, et al. Non-destructive microstructural analysis by electrical conductivity: comparison with hardness measurements in different materials. J Mater Sci Technol 2019;35(3):360–8. https://doi.org/10.1016/j.jmst.2018.09.047.
[32] Santos TG, Vilaa P, Miranda RM. Electrical conductivity field analysis for evaluation of FSW joints in AA6013 and AA7075 alloys. J Mater Process Technol 2011;211(2):174–80. https://doi.org/10.1016/j.jmatprotec.2010.08.030.
[33] Bautista JR, Avilés F, Oliva AI, Ceh O, Corona JE. Correlations between mechanical stress, electrical conductivity and nanostructure in Al films on a polymer substrate. Mater Charact 2010;61(3):325–9. https://doi.org/10.1016/j.matchar.2009.12.016.
[34] Abdo HS, Seikh AH, Mohammed JA, Soliman MS. Alloying elements effects on electrical conductivity and mechanical properties of newly fabricated al based alloys produced by conventional casting process. Materials (Basel) 2021;14(14). https://doi.org/10.3390/ma14143971.
[35] Cui L, et al. Precipitation of metastable phases and its effect on electrical resistivity of Al-0.96Mg2Si alloy during aging. Trans Nonferrous Met Soc China 2014;24(7):2266–74. https://doi.org/10.1016/S1003-6326(14)63343-4.
[36] Bhat MR, Ragupathy VD. Characterisation of friction stir weld discontinuities by non-destructive evaluation. Trans Indian Inst Met 2019;72(11):2971–9. https://doi.org/10.1007/s12666-019-01813-x.
[37] Rosado LS, Santos TG, Ramos PM, Vilaça P, Piedade M. A differential planar eddy currents probe: fundamentals, modeling and experimental evaluation. NDT E Int 2012;51:85–93. https://doi.org/10.1016/j.ndteint.2012.06.010.
[38] Almeida G, Gonzalez J, Rosado L, Vilaça P, Santos TG. Advances in NDT and materials characterization by eddy currents. Procedia CIRP 2013;7:359–64. https://doi.org/10.1016/j.procir.2013.05.061.
[39] Ishkov A, Malikov V. Subminiature Eddy current transducer for inspection of welded joints obtained by friction stir welding. Springer International Publishing 2022. https://doi.org/10.1007/978-3-030-85057-9_44.
[40] Dmitriev SF, Ishkov AV, Katasonov AO, Malikov VN, Sagalakov AM. Investigation of welded joints of aluminium alloys using subminiature eddy-current transducers. IOP Conf Ser Mater Sci Eng 2018;327(3):1–10. https://doi.org/10.1088/1757-899X/327/3/032018.
[41] Smith R. The potential for friction stir weld inspection using transient eddy currents. Insight - Non-Destructive Test Cond Monit 2005;47:133–43. https://doi.org/10.1784/insi.47.3.133.61314.
[42] Brauer H, Otterbach JM, Ziolkowski M, Toepfer H, Graetzel M, Bergmann JP. Friction stir weld inspection using the motion induced eddy current testing technique. AIP Conf Proc 2019;2102. https://doi.org/10.1063/1.5099812.
[43] V. Malikov and A. Ishkov, "Microstructure and Eddy-current analysis of aluminum 01570 welded joints obtained by friction stir welding," Key Eng Mater, vol. 909, pp. 60–69, Feb. 2022, doi:https://doi.org/10.4028/p-n129y8.
[44] Koprivica A, Bajić D, Šibalić N, Vukčević M. Analysis of welding of aluminium alloy AA6082-T6 by TIG, MIG and FSW processes from technological and economic aspect Analysis of welding of aluminium alloy AA6082-T6 by TIG, MIG and FSW processes from technological and economic aspect. Mach Technol Mater 2020;198 (5):194–8.
[45] A. K. Dahle, D. H. S. John, P. Attavanich, and P. Taopetch, "Aluminium alloys - their physical and mechanical properties," Mater Sci Forum, 2000, [Online]. Available: https://api.semanticscholar.org/CorpusID:18667806.
[46] Matweb, "Aluminum 6082-T6." https://www.matweb.com/.
[47] Mauduit A, Gransac H. Study of the precipitation kinetics and mechanisms in 6000 series aluminium alloys through the measurement of electrical conductivity. Ann Chim Sci des Mater 2020;44(3):141–9. https://doi.org/10.18280/acsm.440301.
[48] Arab MA, Mokhtar Z, Blaoui MMB. Experimental investigation on the effect of tool rotational speed on mechanical properties of AA6082-T6 friction stir-welded butt joints. J Fail Anal Prev 2018;18. https://doi.org/10.1007/s11668-018-0562-x.
[49] E. Boldsaikhan, E. Corwin, A. Logar, J. McGough, and W. Arbegast, "Detecting Wormholes in Friction Stir Welds from Welding Feedback Data," *42nd Midwest Instr. Comput. Symp. (MICS* 2009*)*, p. 45 (15 pages), 2009.
[50] Crawford R, Cook GE, Strauss AM, Hartman DA, Stremler MA. Experimental defect analysis and force prediction simulation of high weld pitch friction stir welding. Sci Technol Weld Join 2006;11(6):657–65. https://doi.org/10.1179/174329306X147742.
[51] Kim YG, Fujii H, Tsumura T, Komazaki T, Nakata K. Three defect types in friction stir welding of aluminum die casting alloy. Mater Sci Eng A 2006;415(1–2):250–4. https://doi.org/10.1016/j.msea.2005.09.072.
[52] Serier M, Jassim RJ, Al-Sabur R, Siddiquee AN. Thermal diffusivity modeling for aluminum AA6060 plates during friction stir welding. AIP Conf. Proc. 2024;3051 (1):70004. https://doi.org/10.1063/5.0191742.
[53] Guerra M, Schmidt C, McClure JC, Murr LE, Nunes AC. Flow patterns during friction stir welding. Mater Charact 2002;49(2):95–101. https://doi.org/10.1016/S1044-5803(02)00362-5.
[54] Schmidt H, Hattel J. A local model for the thermomechanical conditions in friction stir welding. Model Simul Mater Sci Eng 2005;13(1):77–93. https://doi.org/10.1088/0965-0393/13/1/006.
[55] Çam G. Friction stir welded structural materials: beyond Al-alloys. Int Mater Rev 2011;56(1):1–48. https://doi.org/10.1179/095066010X12777205875750.
[56] M. Ericsson and R. Sandström, "Influence of welding speed on the fatigue of friction stir welds, and comparison with MIG and TIG," Int J Fatigue, vol. 25, pp. 1379–1387, Dec. 2003, doi:https://doi.org/10.1016/S0142-1123(03)00059-8.
[57] Costa JD, Ferreira JAM, Borrego LP, Abreu LP. Fatigue behaviour of AA6082 friction stir welds under variable loadings. Int. J. Fatigue 2012;37:8–16. https://doi.org/10.1016/j.ijfatigue.2011.10.001.
[58] Yang X, et al. Evolution of microstructure and mechanical properties of cold spray additive manufactured aluminum deposit on copper substrate. Mater Sci Eng A 2024;891:146024. https://doi.org/10.1016/j.msea.2023.146024.
[59] Yang X, et al. A review on linear friction welding of Ni-based superalloys. Int J Miner Metall Mater 2023;31(6):1382–91.
[60] W. J. Arbegast and P. J. Hartley, "Friction stir weld technology development at Lockheed Martin Michoud space systems-An overview," *Proc. 5th Int. Conf. Trends Weld. Res.*, pp. 541–546.
[61] Bush R., Kiyota M., Kiyota C. Characterization of a Friction Stir Weld in Aluminum Alloy 7055 Using Microhardness , Electrical Conductivity , and Differential Scanning Calorimetry (DSC). Metall. Mater. Trans. A 47(7):3522–3532. doi:https://doi.org/10.1007/s11661-016-3506-7.
[62] Sorger G, et al. Non-destructive microstructural analysis by electrical conductivity: comparison with hardness measurements in different materials. J. Mater. Sci. Technol. Sep. 2018;35. https://doi.org/10.1016/j.jmst.2018.09.047.
[63] Verma S, Meenu, Misra JP. Study on temperature distribution during friction stir welding of 6082 aluminum alloy. Mater Today Proc 2017;4, no. 2, Part A:1350–6. https://doi.org/10.1016/j.matpr.2017.01.156.
[64] Xia YJ, Lv TL, Ghassemi-Armaki H, Li YB, Carlson BE. Quantitative interpretation of dynamic resistance signal in resistance spot welding. Weld J 2023;102(4):69–87. https://doi.org/10.29391/2023.102.006.